

## Parameterization of Cloud Microphysics Based on the Prediction of Bulk Ice Particle Properties. Part III: Introduction of Multiple Free Categories

J. A. MILBRANDT

*Atmospheric Numerical Weather Prediction Research, Environment and Climate Change Canada, Dorval, Quebec, Canada*

H. MORRISON

*National Center for Atmospheric Research, Boulder, Colorado*

(Manuscript received 17 July 2015, in final form 16 November 2015)

### ABSTRACT

The predicted particle properties (P3) scheme introduced in Part I of this series represents all ice hydrometeors using a single “free” category, in which the bulk properties evolve smoothly through changes in the prognostic variables, allowing for the representation of any type of ice particle. In this study, P3 has been expanded to include multiple free ice-phase categories allowing particle populations with different sets of bulk properties to coexist, thereby reducing the detrimental effects of property dilution. The modified version of P3 is the first scheme to parameterize ice-phase microphysics using multiple free categories.

The multicategory P3 scheme is described and its overall behavior is illustrated. It is shown using an idealized 1D kinematic model that the overall simulation of total ice mass, reflectivity, and surface precipitation converges with additional categories. The correct treatment of the rime splintering process, which promotes multiple ice modes, is shown to require at least two categories in order to be included without introducing problems associated with property dilution. Squall-line simulations using a 3D dynamical model with one, two, and three ice categories produce reasonable reflectivity structures and precipitation rates compared to radar observations. In the multicategory simulations, ice hydrometeors from different categories and with different bulk properties are shown to coexist at the same points, with effects on reflectivity structure and precipitation. The new scheme thus appears to work reasonably in a full 3D model and is ready to be tested more widely for research and operational applications.

### 1. Introduction

The representation of ice-phase processes in bulk microphysics schemes (BMSs) has advanced considerably over the past 10–20 yr. While in early schemes ice was represented by one or two predefined categories, with prescribed bulk physical properties, and with a single prognostic variable for each (e.g., Rutledge and Hobbs 1983; Lin et al. 1983), many current BMSs now include several ice-phase categories and up to three prognostic moments each in an attempt to model a greater range of particle types and processes (e.g., Straka and Mansell 2005; Milbrandt and Yau 2005a,b;

Seifert and Beheng 2006; Thompson et al. 2008; Morrison et al. 2009; Mansell et al. 2010; Loftus et al. 2014). In the past decade or so there has been a paradigm shift in the representation of ice-phase microphysics away from the continued addition of predefined categories and toward providing more predictive information of the particle properties of the existing (Hashino and Tripoli 2007; Grabowski and Morrison 2008; Mansell et al. 2010; Milbrandt and Morrison 2013; Harrington et al. 2013). This trend is gaining momentum in the model development community.

In Morrison and Milbrandt (2015, hereafter Part I) a new BMS, referred to as the predicted particle properties (P3) scheme, was proposed. This scheme employs a fundamentally different approach to microphysics parameterization whereby all types of ice-phase hydrometeors are represented by a single “free” ice category, where the bulk properties can evolve smoothly and freely with the changes of the prognostic variables on which they depend. This is different than the traditional

Corresponding author address: Dr. Jason A. Milbrandt, Atmospheric Numerical Weather Prediction Research, Environment and Climate Change Canada, 2121 Transcanada Highway, Dorval QC H9P 1J3, Canada.  
E-mail: jason.milbrandt@canada.ca

approach, used in nearly all existing BMSs, which partition ice into several predefined or “fixed” categories with constant parameters corresponding to physical properties of specific types of ice particles. The P3 approach therefore removes the unphysical and inherently problematic conversion between particle types that is necessary in traditional schemes. It was demonstrated in [Part I](#) with idealized 2D mesoscale model simulations that the single-category P3 scheme can realistically simulate a wide range of types of ice particles. It was further shown in [Morrison et al. \(2015\)](#), hereafter [Part II](#), with real-case 3D simulations and comparisons to state-of-the-art BMSs, that the P3 scheme is competitive in terms of overall simulation quality as well as computational efficiency.

For 5 weeks during the 2014 spring, P3 was included among several microphysics schemes in a real-time 4-km ensemble forecast system using the Weather Research and Forecasting (WRF) Model, run by the Center for Analysis and Prediction of Storms (CAPS) at Oklahoma University (F. Kong, personal communication, 2014) in support of the Hazardous Weather Testbed (HWT) Spring Forecasting Experiment, conducted by the National Oceanic and Atmospheric Administration’s National Severe Storms Laboratory and Storm Prediction Center. An informal but expert evaluation of the experiment from five independent groups of participants at the HWT was conducted. It was concluded from comparisons of member runs using different micro-physics schemes but all else identical that forecasts using the [Thompson et al. \(2008\)](#) scheme were generally considered the best overall in terms of the general quality and the guidance for high-impact convective weather events (e.g., storm structure/mode from reflectivity, cloud cover, timing, etc.) but that forecasts with P3 were on par with those using other schemes (A. Clark, personal communication, 2014). It should be noted that all other schemes used during the experiment had been run in real-time settings before and have been tuned and improved over several years, while in contrast this was the first time the P3 scheme had ever been tested in a real-time forecast mode. Similar operational performance for P3 in terms of computational time to that reported in [Part II](#) was noted for the HWT runs. We continue to argue, therefore, that the proposed P3 approach is a conceptual and practical improvement over the traditional approach of using predefined categories and that the new scheme appears to hold considerable promise for both research and operational numerical weather prediction (NWP) applications.

However, despite the ability to model a wide range of ice characteristics with a single category, P3 as described in [Part I](#) and [Part II](#) has the inherent limitation that it is not possible to represent more than one population of

ice particles with different bulk properties at the same point in time and space. In nature two or more modes of ice particles can coexist since populations of particles with different growth histories can arrive at a given point as a result of sedimentation of faster-falling ice from above (i.e., gravitational size sorting), particle recycling (e.g., for hailstones; [Cheng and English 1983](#)), or from in situ ice initiation in the presence of previously existing, larger ice (e.g., rime splintering, drop freezing). When trying to model these processes using a single ice category, mixing of two or more populations of ice—and then representing the sum using a size distribution with a fixed shape (and single mode) and a single set of bulk properties—results in a smoothing or averaging of the properties of the individual ice populations. In essence, therefore, information resulting from different growth histories is lost. This “dilution” effect can be detrimental to the overall simulations since the subsequent growth rates can be changed appreciably as a result of the modified particle properties. For example, consider that at a given location there is ice whose mean size and bulk density is representative of large graupel. If there is in situ nucleation of new, tiny crystals, the total local ice mass may not change much but the number concentration may increase appreciably such that the mean size, fall speed, etc., are significantly decreased. The dilution thus alters the subsequent evolution of the previously existing heavily rimed ice. To minimize this effect and to allow for a better representation of the real processes of combining existing particle populations, two or more ice-phase categories are clearly required.

To this end, the P3 scheme has been expanded to allow for multiple free ice-phase categories. For each category, the same wide range of possible particle properties exists as in the original scheme, however multiple modes now are possible at the same point in time and space, removing the intrinsic limitation of the original one-category version of the scheme and thereby improving its overall capacity to simulate microphysical processes. This is the first time this approach to model ice-phase microphysics has been attempted. In this study, the modified version of P3 is described and the effects of using multiple categories are illustrated in the context of idealized 1D and quasi-idealized 3D model simulations.

The remainder of this article is organized as follows. The modifications to the original scheme are described in the following section. In [section 3](#), the effects of the generalized approach are illustrated in the context of an idealized 1D kinematic model. In [section 4](#), the behavior of the multicategory scheme configuration is further examined using 3D mesoscale model simulations. Discussion and concluding remarks are given in [section 5](#).

TABLE 1. List of symbols.

Symbol	Description	Units
$\rho_{\text{rim}}$	Rime density	$\text{kg m}^{-3}$
$B_{i,\text{rim}}(n)$	Rime volume mixing ratio for ice category $n$	$\text{m}^3 \text{kg}^{-1}$
$D_i(n)$	Mean-mass diameter for ice category $n$	m
$D_{\text{new}}$	Diameter of new ice	m
$E_{j,k}$	Collection efficiency among ice	—
$F_{\text{rim}}(n)$	Rime mass fraction for ice category $n$	—
$n$	Ice category index	—
$n_{\text{Dest}}$	Ice category index for new ice	—
$n_{\text{Cat}}$	Number of ice categories	—
$N_{i,\text{tot}}(n)$	Total number mixing ratio for ice category $n$	$\text{kg}^{-1}$
$N_{i,\text{total}}$	Total number mixing ratio for ice for all categories	$\text{kg}^{-1}$
$\Delta D_{\text{init}}$	Diameter difference threshold for ice initiation	m
$Q_{i,\text{rim}}(n)$	Rime mass mixing ratio for ice category $n$	$\text{kg kg}^{-1}$
$Q_{i,\text{tot}}(n)$	Total mass mixing ratio for ice category $n$	$\text{kg kg}^{-1}$
$Q_{i,\text{total}}$	Total mass mixing ratio for ice of all categories	$\text{kg kg}^{-1}$
$V_i(n)$	Mass-weighted fall speed for ice category $n$	$\text{m s}^{-1}$
$w_{\text{max}}$	Peak updraft speed	$\text{m s}^{-1}$
$Z_e$	Equivalent reflectivity	dBZ

## 2. Description of the multicategory scheme

### a. Summary of one-category version

A complete description of the one-category version of P3 is given in Part I. A brief overview of the treatment of the ice phase is provided here to facilitate the description of the changes for the multicategory version. All symbols used in this paper are summarized in Table 1.

In the original scheme, all ice-phase hydrometeors are represented by a single free category, with four prognostic variables— $Q_{i,\text{tot}}$ ,  $Q_{i,\text{rim}}$ ,  $N_{i,\text{tot}}$ , and  $B_{i,\text{rim}}$ —and a complete gamma size distribution function. The two mass mixing ratios allow for the independent prediction of mass from vapor deposition and from riming of liquid water. The inclusion of  $B_{i,\text{rim}}$  as a prognostic variable allows for the prediction of the rime density (given by the ratio  $Q_{i,\text{rim}}/B_{i,\text{rim}}$ ). At each time step, the size distribution parameters for existing ice are computed as well as the mass-size, area-size, and fall speed-size parameters for various size intervals. Ice initiation rates are computed for various nucleation modes as well as rates of growth and decay, which include interaction with water vapor (deposition–sublimation), interactions with liquid water (riming), and interactions with existing ice (self-collection). The prognostic variables are then updated from the sum of the process rates. Finally, sedimentation is computed

based on these intermediate values to obtain the final values of each prognostic ice variable at the end of the microphysics step.

### b. New elements for the multicategory version

In the generalized scheme, ice is now distributed among  $n_{\text{Cat}}$  free categories. Each category is treated essentially the same as in the one-category version in that it can evolve freely according to the environmental conditions and can represent any type of ice-phase particle, based on its derived physical properties. What is different is that at a given point in time and space there can now be more than one “mode” of particles, or subpopulations with different bulk properties, owing to the possible presence of ice from more than one category.

In the scheme itself, the number of ice categories used for a given simulation is determined by the user-specified value of the parameter  $n_{\text{Cat}}$ , which can be any integer (1 or greater). The prognostic variable arrays  $Q_{i,\text{tot}}$ ,  $Q_{i,\text{rim}}$ ,  $N_{i,\text{tot}}$ , and  $B_{i,\text{rim}}$  now have an additional dimension of  $n_{\text{Cat}}$ . For both the ice-phase process rates and sedimentation sections of the scheme, all computations are now done within a loop around  $n_{\text{Cat}}$ . The destination category upon initiation of new ice must first be determined appropriately. Collection among the various ice-phase categories is also computed. Finally, categories with similar ice properties are merged in order to make available an empty category for subsequent possible ice initiation. These new aspects are elaborated upon below. No assumptions or specifications of any kind are made to predefined any particular category.

#### 1) DETERMINATION OF THE DESTINATION CATEGORY OF NEW ICE

The purpose of having more than one category is ultimately to minimize the dilution effect discussed above. Except for the extreme situation in which the properties of the newly nucleated particles are identical to the previously existing ones, initiation of new ice into an existing population of ice represented by a P3 category will always result in some degree of dilution. The greater the number of categories, the less dilution there is. For a finite  $n_{\text{Cat}} > 1$ , in order to minimize the amount of dilution and thereby maximize the utility of the existing categories it is necessary to select the destination category of newly initiated ice appropriately.

To accomplish this, we consider the mean-mass ice particle size,  $D_i$ , of the newly initiated ice and of the ice present in the existing category(ies) when determining the destination category. While dilution

implies the general smoothing of bulk particle properties, we focus specifically on  $D_i$  since it is directly important for fall speeds and growth rates and is useful to delineate different particle size modes, which indicates populations with different origins. The size is not the only physical property that could be used, and in fact it can fail to delineate some sets of particle modes. For example, ice that is characteristic of aggregates of dendrites could have a similar mean size as ice characteristic of hail. However, the use of  $D_i$  is generally effective for determining the destination category with the intended purpose of minimizing the overall dilution, as shown below. Other properties or environmental conditions may be explored in the future.

If no ice is present in any category, ice is simply initiated into the first category. If ice is already present in one or more of the existing categories, then to determine the destination category—either one of the populated categories or a category with zero content if one is available—the difference in  $D_i$  between the nucleated ice and the existing ice in each category is first computed. Note that the size of new ice depends on the initiation mode: for heterogeneous nucleation by deposition or condensation freezing and for ice formed from rime splintering it is assumed that the size of new

ice is  $10\text{ }\mu\text{m}$ ; for ice formed from frozen cloud droplets the  $D_i$  values are around  $10\text{--}30\text{ }\mu\text{m}$ ; ice from frozen raindrops can have mean sizes approaching  $1\text{ mm}$ . If all categories are populated, then the destination category is that with the smallest difference in  $D_i$ . The physical reasoning is that this is the category with existing ice that has the closest properties to the new ice, and thus the minimum possible dilution is introduced. If there is at least one empty category, then the first available category is used provided that the minimum difference with the existing categories exceeds a difference threshold ( $\Delta D_{\text{init}}$ ); otherwise ice is initiated into the category with the smallest difference. The effects of specific values of  $\Delta D_{\text{init}}$  for initiation are examined in more detail below.

## 2) COLLECTION AMONG ICE-PHASE CATEGORIES

Collection between categories is based on a gravitational collection kernel integrated over the size distributions of the two interacting categories. Transfer of the prognostic variables between categories is determined by the fall speed difference between the categories for a given  $D$ , with transfer from the category with the smaller fall speed to that with the larger fall speed. Thus, it is formulated as

$$\frac{\partial X_{j,k}}{\partial t} = \int_0^{\infty} \int_0^{\infty} \rho E_{j,k} (A_j + A_k) G(V_j - V_k) Y_k N_j(D_j) N_k(D_k) dD_j dD_k \quad \text{and} \quad (1)$$

$$\frac{\partial X_{k,j}}{\partial t} = \int_0^{\infty} \int_0^{\infty} \rho E_{j,k} (A_j + A_k) G(V_k - V_j) Y_j N_j(D_j) N_k(D_k) dD_j dD_k,$$

where  $X$  is the prognostic quantity that is being transferred ( $Q_{i,\text{tot}}$ ,  $Q_{i,\text{rim}}$ ,  $N_{i,\text{tot}}$ , or  $B_{i,\text{rim}}$ );  $\rho$  is the air density;  $E_{j,k}$  is the collection efficiency;  $A$  and  $V$  are the particle projected areas and fall speeds, respectively, as a function of  $D$ ;  $N(D)$  is the size distribution; and  $j$  and  $k$  are indices denoting the two interacting categories. Here  $G$  is a selection function that is zero when the argument is negative and equal to the argument when it is positive. The first subscript of  $X$  denotes the category gaining from collection while the second subscript denotes the category with loss. The  $Y$  depends on the quantity being transferred and is equal to 1,  $m$ ,  $mF_{\text{rim}}$ , and  $mF_{\text{rim}}\rho_{\text{rim}}$  for the transfer of  $N_{i,\text{tot}}$ ,  $Q_{i,\text{tot}}$ ,  $Q_{i,\text{rim}}$ , and  $B_{i,\text{rim}}$ , respectively, where  $m$ ,  $F_{\text{rim}}$ , and  $\rho_{\text{rim}}$ , are the mass, rime mass fraction, and rime density of the collected particles, respectively. Because of the computational cost of calculating the double

integral in (1), it is precomputed numerically and values are stored in a lookup table.

The collection efficiency,  $E_{j,k}$ , is an uncertain quantity although there is observational evidence of a temperature dependency and that values around 0.1 for ice crystals are reasonable (Pruppacher and Klett 1997). Further comments regarding this assumption are made in section 3d. Graupel and hail, on the other hand, undergo less collection of or by any frozen hydrometeors. For simplicity in the current version of the scheme, collection involving graupel/hail is assumed to be negligible. To suppress collection involving heavily rimed particles,  $F_{\text{rim}}$  and  $V_i$  are used to diagnose particles as being graupel-like. The value of  $E_{j,k}$  is 0.1 but tends linearly to 0 for  $V_i$  values of the collector category between 1 and  $2\text{ m s}^{-1}$  whenever  $F_{\text{rim}} > 0.5$ . Alternative approaches that allow for

collection involving rimed ice will be explored in future work.

### 3) MERGING OF CATEGORIES WITH SIMILAR ICE PROPERTIES

As described above, if all available categories contain ice at the beginning of the time step new ice must be placed into one of the existing categories, for a given nCat. This has the potential to result in an undesirable amount of dilution of the ice properties in that category, as illustrated below in section 3d. It is possible in such situations that the existing ice in two given categories may in fact be more similar in properties than the new ice and the ice in the destination category. Thus, less overall dilution would result if those existing categories were merged, thereby creating an empty available category for newly initiated ice.

To accomplish this, a general merging of categories containing ice with similar properties is done at the end of the microphysics step, immediately following sedimentation. In the current version of the generalized scheme, the conditions that ice in two categories are considered similar enough that they are to be merged is that the difference in mean-mass diameters is less than  $150\text{ }\mu\text{m}$  and the difference in bulk densities is less than  $100\text{ kg m}^{-3}$ . The ice in each category is compared to that in each of the other categories; if both of these conditions are met, the ice is merged into a single category by summing each of the prognostic variables, assigning these values to one of the categories, and setting values of zero to the other. At the following time step, newly initiated ice is more likely to have an empty category into which to be placed, thereby reducing the overall dilution.

The merging condition is selected subjectively in an attempt to encompass the overall similarity of populations of ice that have sufficiently similar properties. As such, some sensitivity to the solution is introduced. Other conditions for merging, as well as other properties or conditions to determine the destination category of new ice, may be explored. However, this sensitivity only affects the degree to which the existing ice categories are used efficiently to reduce overall dilution.

#### c. Interfacing with driving model

The driving model must have additional prognostic (i.e., advected) variables, four for each additional ice category. In a dynamical model, for each category  $n$ ,  $Q_{i,\text{tot}}(n)$  must be included for mass loading;  $Q_{i,\text{rim}}(n)$  is excluded since  $Q_{i,\text{rim}}(n)$  is a subset of the total ice mass  $Q_{i,\text{tot}}(n)$ . Note that each  $Q_{i,\text{tot}}(n)$  represents only the total mass for category  $n$ ; in the multicategory version the total ice mass of all categories,  $Q_{i,\text{total}}$ , is the sum of all  $Q_{i,\text{tot}}(n)$ .

The calculation of cloud optical properties must be done with some care since radiative transfer schemes often assume only a single ice mode (e.g., Li and Barker 2005). Examination of the sensitivity to the correct calculation of cloud optical properties for P3 with nCat > 1 in a full dynamical model is beyond the scope of this article.

## 3. Idealized 1D simulations

### a. Effects of multiple categories

To illustrate the general behavior of P3 with different numbers of ice categories, simulations are performed using a 1D kinematic driving model. In this simple idealized framework, the updraft profile can be controlled in order to mimic different degrees of the environmental forcing that could exist in a 3D dynamical model. Details of the 1D model are provided in Milbrandt et al. (2014). For the following tests, temperature and humidity are initialized using a sounding that would support deep convection (Fig. 1a). A time-varying vertical motion profile is prescribed as a half sine wave which increases in vertical extent and peak magnitude, reaching its maximum values at 30 min, and then decreases to zero by 60 min with no vertical air motion thereafter (Fig. 1b). The profiles of the various predicted fields are output each time step in order to construct Hovmöller diagrams.

Results from 1D simulations are presented to illustrate the behavior using what we refer to as the control (CTR) configuration of the generalized P3 scheme, with all parameterized microphysical processes switched on and a constant value of  $500\text{ }\mu\text{m}$  for  $\Delta D_{\text{init}}$ . Sensitivity tests and a final proposed scheme configuration are discussed in the sections that follow.

The time–height plots in Fig. 2 summarize a simulation with a peak vertical motion ( $w_{\text{max}}$ ) of  $10\text{ m s}^{-1}$  with the CTR configuration and nCat = 1. The figure shows the evolution, for the one-category configuration, of  $Q_{i,\text{tot}}$ ,  $N_{i,\text{tot}}$ ,  $F_{\text{rim}}$ , the mass-weighted mean particle density ( $\rho_i$ ),  $D_i$ , and  $V_i$ , where the latter four fields are computed from the appropriate prognostic quantities (see Part I for details). Liquid cloud water (not shown) forms first in the updraft core after which ice forms, grows quickly by riming, is transported aloft, and then falls toward the surface as the updraft decreases and the bulk ice fall speed exceeds the vertical air velocity. A considerable amount of information about the ice particle characteristics is available from the scheme, shown in the figure. For example, where the ice mass is greatest, the ice exhibits properties of large, heavily rimed, and relatively low-density particles ( $<150\text{ kg m}^{-3}$ ). In contrast, at

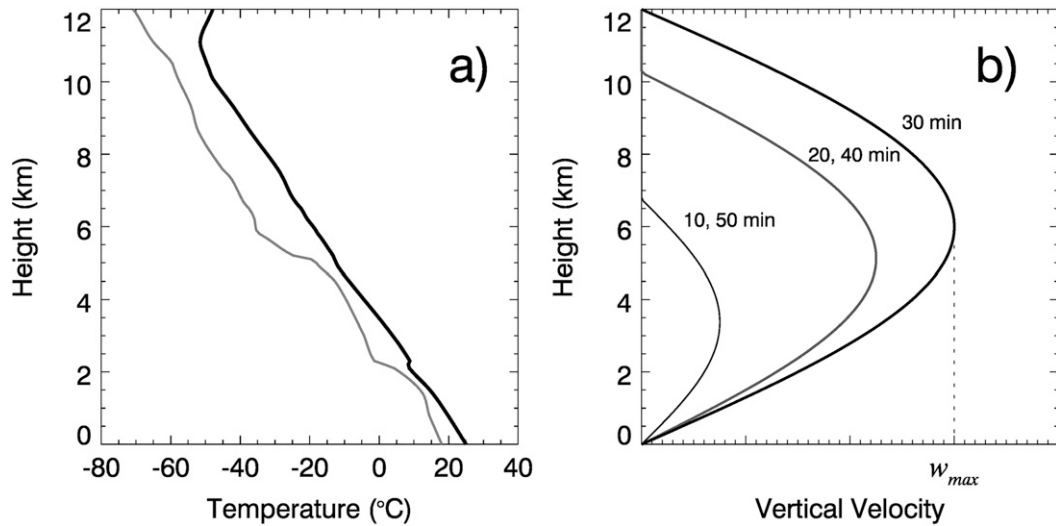


FIG. 1. (a) Initial profiles of temperature (thick) and dewpoint temperature (thin) and (b) updraft provided at various integration times for the 1D kinematic model simulations.

upper levels the ice is characteristic of tiny crystals, with large number concentrations, smaller mean sizes, higher density, and it is composed primarily of deposition mass. This is the overall behavior of the one-category P3 scheme in the 1D model with strong vertical motion imposed. Note, while a peak updraft speed of  $10 \text{ m s}^{-1}$  is small compared to that observed in continental convective storms, whose peak updraft speeds can easily exceed  $30 \text{ m s}^{-1}$  (e.g., Yuter and Houze 1995), the 1D kinematic framework is highly idealized and lacks processes such as entrainment of dry air, buoyancy loading, etc. Thus,  $w_{max} = 10 \text{ m s}^{-1}$  in this idealized framework should be interpreted as a strong updraft. Similar results were found using  $w_{max} = 20 \text{ m s}^{-1}$  (not shown).

The simulation with the same setup but now with two ice categories is summarized in Fig. 3, with the predicted fields from each category shown. It is immediately evident that at any given point the properties of ice differ for the different categories. For example, at 5 km after 60 min, the ice in category 1 has a high mass content ( $\sim 20 \text{ g kg}^{-1}$ ), nearly all of which is rime mass ( $F_{\text{rim}} \sim 1$ ), moderate number concentrations ( $N_{i,\text{tot}} \sim 104 \text{ kg}^{-1}$ ), low density ( $< 150 \text{ kg m}^{-3}$ ), moderately large size ( $\sim 4 \text{ mm}$ ), and moderate fall speed ( $\sim 3 \text{ m s}^{-1}$ ). In contrast, at that same point in time and space the ice in category 2 has much lower mass, higher concentration, lower rime mass fraction ( $F_{\text{rim}} \sim 0$ ), is small, and has low fall speeds ( $< 0.5 \text{ m s}^{-1}$ ). Thus, with two free categories the generalized scheme is capable of simulating populations or “modes” of ice with different bulk physical properties at the same time and location. Furthermore, this changes the simulation results. For example, with  $n\text{Cat} = 1$  the majority of the ice mass arrives near the

surface (before melting) at approximately 90 min (Fig. 2a) but it arrives earlier ( $\sim 70 \text{ min}$ ) with  $n\text{Cat} = 2$  (Fig. 3a). This change occurs because of a reduction in the dilution effect with the  $n\text{Cat} = 2$  simulation, which is evident by the relatively low number concentrations of ice in category 1 (Fig. 3c), which allows ice in this category to grow to larger sizes and have faster fall speeds (Fig. 3k) than the ice with  $n\text{Cat} = 1$  (Fig. 2f).

The simulation with  $n\text{Cat} = 3$  is shown in Fig. 4. Given that relatively little ice appears in category 3 with the scheme configuration used (Fig. 4c), the results are very similar to the  $n\text{Cat} = 2$  results. This changes notably, however, when  $\Delta D_{\text{init}}$  is modified (discussed below). The results of these three simulations are summarized in Fig. 5, now with plots of the total (from all categories) ice masses (Figs. 5a–d) and total number concentrations (Figs. 5e–h) from a given run, along with the equivalent reflectivities ( $Z_e$ ; Figs. 5i–l) and surface liquid and solid precipitation rates (Figs. 5m–p). In the CTR configuration, simulations with  $n\text{Cat} \geq 4$  (not shown) are identical to the  $n\text{Cat} = 3$  simulation since no new ice is ever initiated into the fourth and higher categories. The set of simulations was repeated using the CTR configuration with different values of  $n\text{Cat}$  but with weaker implied forcing by imposing  $w_{max} = 3 \text{ m s}^{-1}$  (Fig. 6).

Some general trends are evident from the simulations discussed up to this point. As the number of ice categories is increased, the time it takes for a majority of the ice mass to reach the melting layer is reduced, as is the corresponding onset of liquid precipitation at the surface. This is consistent with what one would hypothesize given that with more categories there should be less overall dilution. The maximum total ice mass quantities

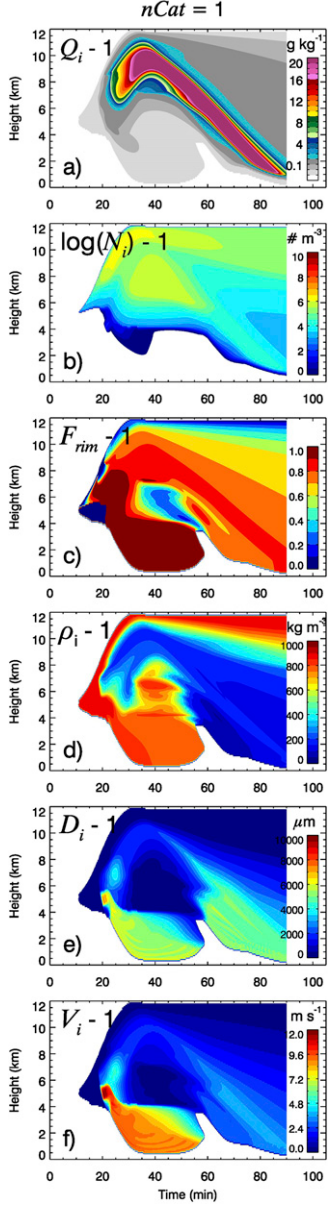


FIG. 2. Simulation from 1D kinematic model with  $w_{\max} = 10 \text{ m s}^{-1}$  and  $n\text{Cat} = 1$ . Shown are (a)  $Q_{i,\text{tot}}$ , (b)  $N_{i,\text{tot}}$ , (c)  $F_{\text{rim}}$ , (d)  $\rho_i$ , (e)  $D_i$ , and (f)  $V_i$ . The shaded values in (a) denote  $Q_i$  values of  $0.001, 0.01, 0.1, 1, 2, \dots \text{ g kg}^{-1}$ , with the values of  $\geq 1 \text{ g kg}^{-1}$  starting with the light blue. The number after the variable symbol in the top-left corner of each panel denotes the ice category number.

are also lower with higher  $n\text{Cat}$ . Further, for the simulated precipitation rates as well as the overall patterns of total ice mass, total ice number, and reflectivity, there is a “convergence” in the solutions, in that the overall simulated fields become similar with increased values of  $n\text{Cat}$ , since at some point ice is never initiated into the next available category. The value of  $n\text{Cat}$  at which this

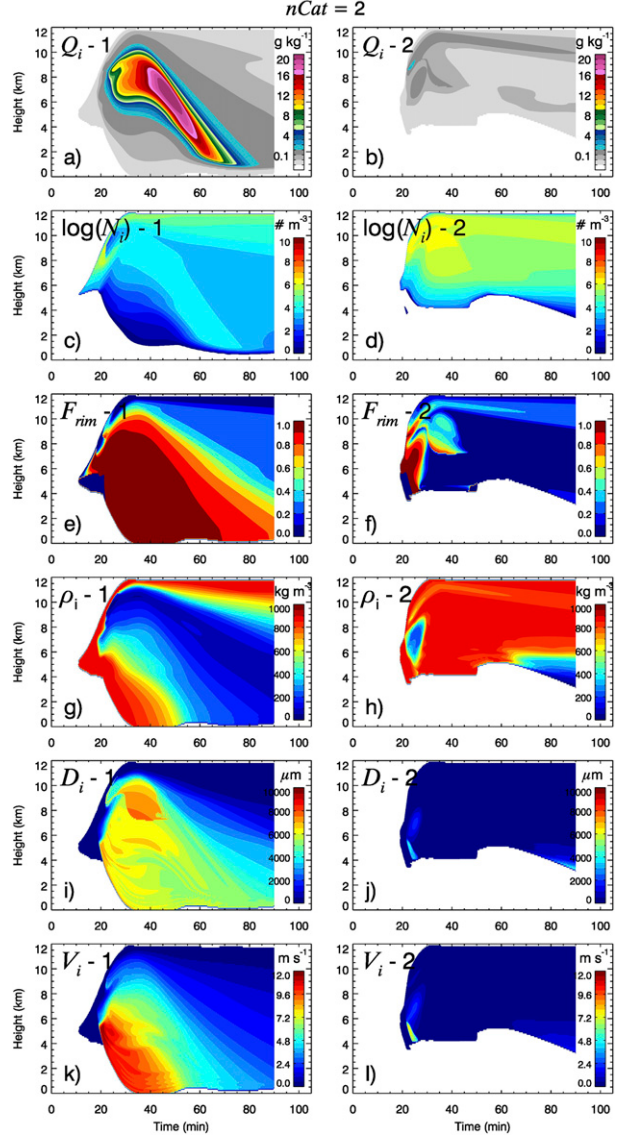


FIG. 3. As in Fig. 2, but for  $n\text{Cat} = 2$ .

convergence occurs is higher for cases with stronger upward motion; approximate convergence occurs at  $n\text{Cat} = 3$  for  $w_{\max} = 10 \text{ m s}^{-1}$  and at  $n\text{Cat} = 2$  for  $w_{\max} = 3 \text{ m s}^{-1}$ .

Note that for these simulations with the CTR configuration, the convergence that occurs when ice is no longer initiated into an available category (with no existing ice) is related to the use of the same value of the  $\Delta D_{\text{init}}$  parameter regardless of the number of categories. This changes when  $\Delta D_{\text{init}}$  is set to be a decreasing function of  $n\text{Cat}$ , as is discussed below. Overall, the generalized P3 scheme appears to produce the expected results and the use of multiple ice categories does indeed change the overall simulation, reducing the detrimental

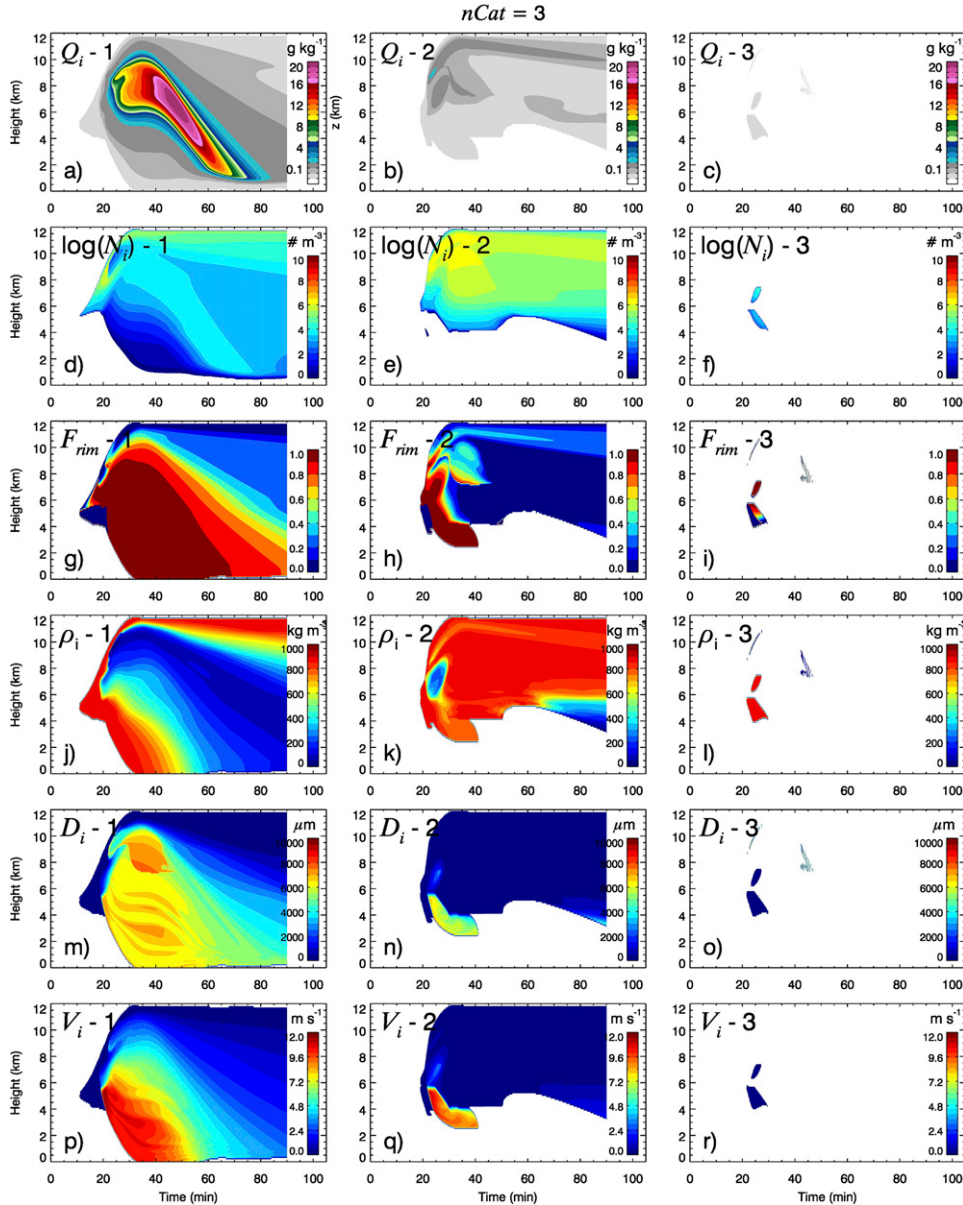


FIG. 4. As in Fig. 2, but for nCat = 3.

effects of the dilution of ice particle properties by using two or more categories.

#### b. Sensitivity to the destination category of new ice

The results discussed in the previous subsection used the CTR configuration, with  $\Delta D_{\text{init}} = 500 \mu\text{m}$  and all physical processes on. As discussed in section 2,  $\Delta D_{\text{init}}$  affects the amount of dilution and should depend in part on nCat. Before discussing 1D simulation results with modified  $\Delta D_{\text{init}}$ , we return briefly to some conceptual considerations of the effects of its specific values in different situations involving initiation of new ice. Some

illustrations of the effects of  $\Delta D_{\text{init}}$  are given in Table 2. For example, as illustrated in the fourth row, new ice with a  $D_i$  of  $10 \mu\text{m}$  is initiated into category 2, with the existing ice having a mean-mass size of  $400 \mu\text{m}$ , resulting in considerable dilution as indicated by the size after mixing of  $46.6 \mu\text{m}$ . However, reducing  $\Delta D_{\text{init}}$  from 500 to  $300 \mu\text{m}$  for this initial mixing scenario (fifth row) results in new ice being initiated into a new (third) category, thereby reducing the dilution effect. In the cases where all categories are already populated, some dilution is inevitable upon new ice initiation (rows 6 and 7).

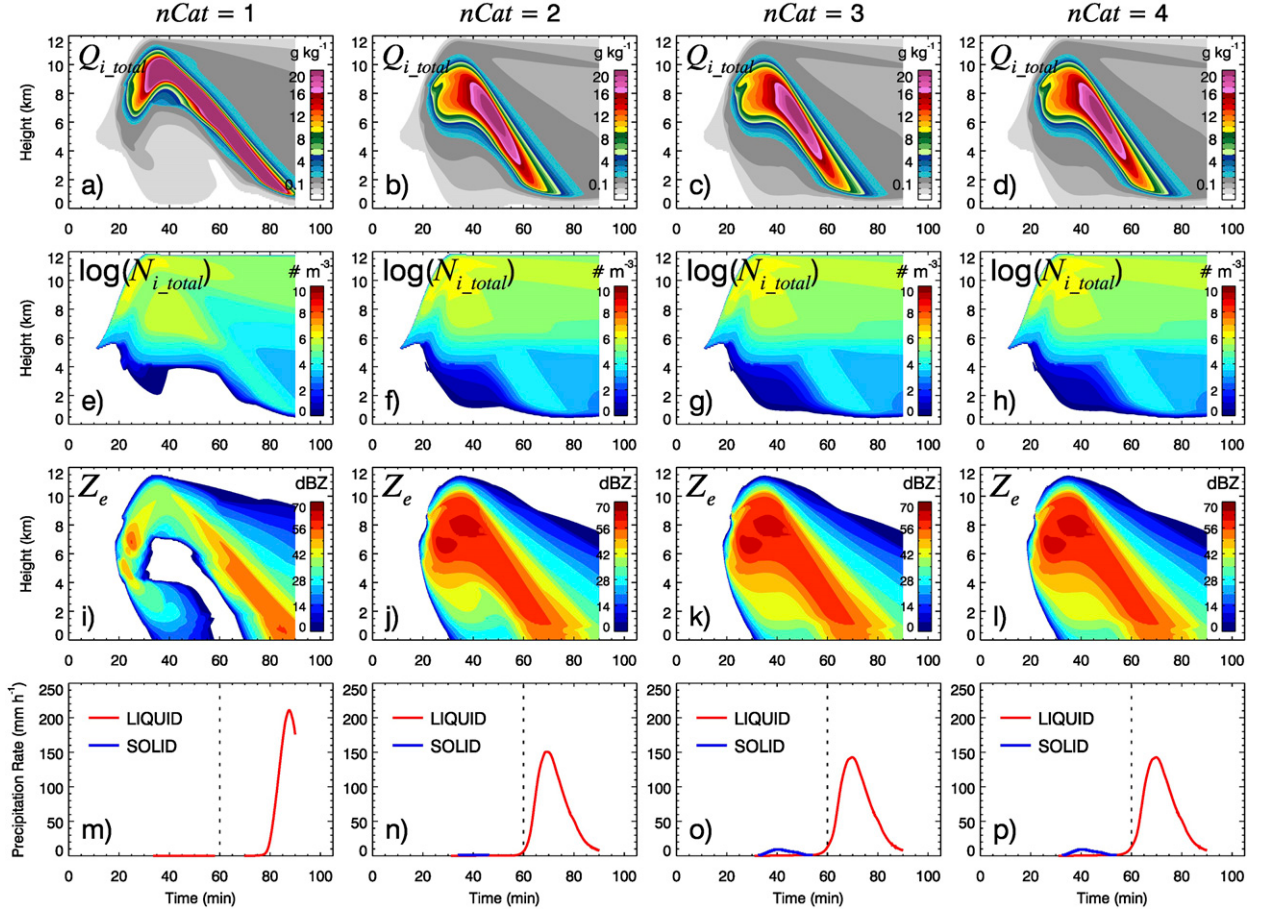
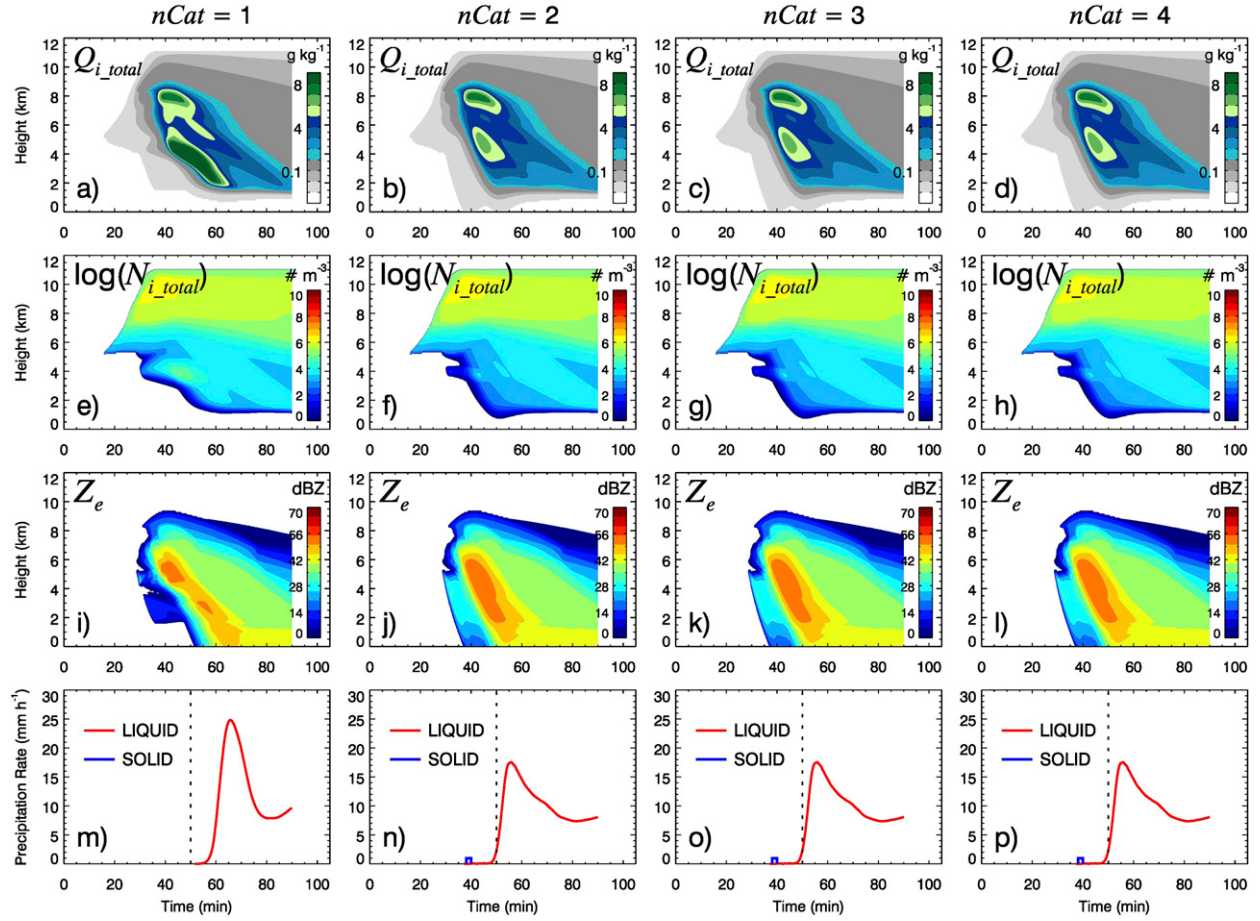


FIG. 5. Simulations vs time from 1D kinematic model with  $w_{\max} = 10 \text{ m s}^{-1}$  and (left to right)  $n\text{Cat} = 1, 2, 3, 4$  and (a)–(d)  $Q_{i,\text{tot}}$ , (e)–(h)  $N_{i,\text{tot}}$ , (i)–(l)  $Z_e$ , and (m)–(p) liquid and solid surface precipitation rates.

Although the value of  $\Delta D_{\text{init}}$  is of some importance, specifying it poorly simply reduces the utility of additional categories, in effect making P3 behave as though  $n\text{Cat}$  were smaller. If  $\Delta D_{\text{init}}$  is larger than the maximum possible mean size difference between new and existing ice, then all ice would be nucleated into the first category and thus the solution would be identical to that using  $n\text{Cat} = 1$ . At the other extreme, if  $\Delta D_{\text{init}} = 0$ , then all categories populate quickly and evolve similarly (but not necessarily equally, owing to small differences that can grow over time), with an overall simulation very similar to that of  $n\text{Cat} = 1$ . The ideal value of  $\Delta D_{\text{init}}$  depends on the value of  $n\text{Cat}$  and should be smaller with increasing number of categories. Given that stronger forcing for ice initiation and growth will tend to populate more categories, as illustrated in section 3, the ideal value of  $\Delta D_{\text{init}}$  should also depend on the type of case if one wishes to maximize the utility of all ice categories.

Here, a trial-and-error procedure to determine the ideal  $\Delta D_{\text{init}}$  as a function of  $n\text{Cat}$  was used based on the

1D simulations using the strong upward motion case ( $w_{\max} = 10 \text{ m s}^{-1}$ ). For application in a particular 3D modeling context, this type of procedure should be performed again to improve the specification of  $\Delta D_{\text{init}}$ , with the recognition of situational dependence. It should be stressed that no harm is done, per se, if the value of  $\Delta D_{\text{init}}$  used is not ideal; it just means the use of the existing ice categories in a simulation with P3 is suboptimal. For example, in the fourth row of Table 2,  $D_{\text{new}} = 10 \mu\text{m}$  and although there is an empty ice category available, the new ice is initiated into category 2, thereby reducing the mean size from 400 to  $46.6 \mu\text{m}$ . However, by reducing  $\Delta D_{\text{init}}$  from 500 to  $300 \mu\text{m}$  (fifth row in Table 2), new ice is now initiated into category 3, and category 2 does not experience dilution. In the worst (most poorly specified) possible cases, either with  $\Delta D_{\text{init}}$  set larger than the largest possible initial ice size or with  $\Delta D_{\text{init}} = 0$ , the scheme simply reverts to its one-category behavior. This solution is identical to the one-category configuration for the first extreme case since no ice is

FIG. 6. As in Fig. 5, but for  $w_{\max} = 3 \text{ m s}^{-1}$ .

ever initiated into any of the other categories, whereas for the second extreme case the categories become populated approximately equally, resulting in maximum dilution and thus an overall solution similar to  $nCat = 1$ , but with the total ice distributed among the categories. As such,  $\Delta D_{\text{init}}$  is not simply a tuning parameter, such as ad hoc conversion thresholds used in traditional micro-physics schemes or a fixed physical constant such as a fall speed parameter, since  $\Delta D_{\text{init}}$  does not appear in any of the parametric equations; the value of  $\Delta D_{\text{init}}$  just affects the way ice is distributed among the free categories. The same argument applies to the condition for the merging of categories containing ice with similar properties described above.

The 1D model was rerun with  $w_{\max} = 10 \text{ m s}^{-1}$  and  $nCat$  ranging from 2 to 6, each with different values of  $\Delta D_{\text{init}}$ . For a given  $nCat$ , the ideal value of  $\Delta D_{\text{init}}$  was determined by inspection of the various simulations and selecting the run that exhibited the least amount of dilution. This evaluation is subjective, but it is also quite clear; all categories should ideally have some ice and

with the last category having a significantly smaller but still nonnegligible ice content. This implies that since ice was initiated into the last category the dilution was minimized in the other categories and that the last category itself likely experienced the lowest amount of dilution possible for the given number of categories. Based on this procedure, the ideal values of  $\Delta D_{\text{init}}$  that were determined for each  $nCat$  are indicated in the plot in Fig. 7. The shape of the curve is as one would expect, such that the optimal value of  $\Delta D_{\text{init}}$  decreases with increasing  $nCat$  but to a lesser degree with each additional category as  $nCat$  becomes larger.

For the simulations with  $w_{\max} = 10 \text{ m s}^{-1}$  using these ideal  $\Delta D_{\text{init}}$  values, the total ice mass and number for each category are shown for  $nCat = 2, 3$ , and  $4$  in Fig. 8. For each configuration, only a small quantity of mass is present in the last category (Figs. 8b,g,n). Note that these simulations differ somewhat from the runs with the  $\Delta D_{\text{init}} = 500 \mu\text{m}$  CTR configuration (Figs. 3 and 4). Figure 9 shows summary plots for the total (of all

TABLE 2. Example of determination of the destination ice category ( $n_{\text{Dest}}$ ) for a given value of  $\Delta D_{\text{init}}$  and the sizes of the new ice ( $D_{\text{new}}$ ) and the ice already present in each category ( $D_{n^0}$ ). The size difference between ice in each destination category and the new ice is indicated parenthetically. A “—” indicates that no ice is present in that category. For all examples,  $n_{\text{Cat}} = 3$ . The three rightmost columns indicate the sizes in each category after the new ice mass (if applicable) has been added ( $D_{n^+}$ ), assuming the new ice is 1/1000 of the existing mass and all ice spherical with the same density. All sizes are in  $\mu\text{m}$ .

$\Delta D_{\text{init}}$	$D_{\text{new}}$	$D_{1^0}(\text{diff})$	$D_{2^0}(\text{diff})$	$D_{3^0}(\text{diff})$	$n_{\text{Dest}}$	$D_{1^+}$	$D_{2^+}$	$D_{3^+}$
500	10	—	—	—	1	10	—	—
500	10	15 (5)	—	—	1	14.99	—	—
500	10	600 (590)	—	—	2	600	10	—
500	10	600 (590)	400 (390)	—	2	600	99.5	—
300	10	600 (590)	400 (390)	—	3	600	400	10
300	700	600 (100)	400 (200)	—	1	600.07	400	—
300	10	600 (590)	400 (390)	350 (340)	3	600	400	99.26
300	700	500 (100)	400 (300)	350 (350)	1	500.1	400	350

categories) ice mass, number, reflectivity, and surface precipitation rates for  $n_{\text{Cat}}$  from 2 to 6 as well as the  $n_{\text{Cat}} = 1$  run with the CTR configuration (all processes on). For the overall patterns of these fields, there is an approximate convergence in the solutions at  $n_{\text{Cat}} = 4$  (Figs. 9n,q,t,w), although the liquid precipitation rate differs for  $n_{\text{Cat}} = 6$  (Fig. 9x). This is different than in the CTR configuration runs (Fig. 5) where the approximate convergence occurred with  $n_{\text{Cat}} = 3$  and resulted from no new ice being initiated into the last category with  $n_{\text{Cat}} > 3$ . With the new runs, although there is convergence in the overall solutions, the fields for the individual ice categories are different between the  $n_{\text{Cat}} = 5$  and  $n_{\text{Cat}} = 6$  runs (not shown). This illustrates that because of the appropriate value of  $\Delta D_{\text{init}}$ , it does not ultimately add any appreciable value to increase the number of categories beyond 5, although all categories are used effectively with  $n_{\text{Cat}} = 6$ . It is reasonable to expect a similar convergence in the context of a 3D dynamical model.

Using the same  $\Delta D_{\text{init}} = f(n_{\text{Cat}})$  functional relation, simulations with  $w_{\text{max}} = 3 \text{ m s}^{-1}$  were conducted (Figs. 10 and 11). It is evident from the lack of ice content in the last categories (e.g., Figs. 10g,n) that the values of  $\Delta D_{\text{init}}$  are not ideal for this more weakly forced case. Again, this is not particularly detrimental as is evident, for example, by the fact that the overall solutions with  $\Delta D_{\text{init}} = 3$  and  $n_{\text{Cat}} = 6$  (which has ice in all categories; not shown) are very similar; it just means that the model does not make optimal use of the available categories. With this weakly forced case, approximate convergence occurs with  $n_{\text{Cat}} = 2$ . However, the evolution of surface precipitation rates, though not the timing of precipitation onset, is sensitive to small changes in this idealized context, given that there are the changes in the rates for the higher  $n_{\text{Cat}}$  simulations for both  $w_{\text{max}} = 10 \text{ m s}^{-1}$  (Fig. 9x) and  $w_{\text{max}} = 3 \text{ m s}^{-1}$  (Figs. 11w,x).

### c. Effects of ice multiplication

Initiation of new ice at a location where ice is present and all categories already populated invariably results in a dilution effect, which can in some cases be severe (e.g., Table 2, row 7). Part of this problem can be regarded as a result of attempting to model the microphysical processes beyond the intrinsic limitations of a particular P3 configuration, where few or only one ice category is used. Since for some modeling applications the use of few categories may be necessary (e.g., whenever computational cost is an issue) and dilution is always potentially detrimental, the problem may be mitigated by simply neglecting certain processes. Consider the process of rime splintering (Hallett and Mossop 1974). The effect of this process is quite noticeable in the 1D simulations with the weak updraft (Figs. 6 and 11), where there is a pronounced increase in  $N_{i\_total}$  at an elevation of 4 km after approximately 30 min (for all  $n_{\text{Cat}}$  runs). As discussed, the  $n_{\text{Cat}} = 1$  simulation also clearly suffers from detrimental dilution effects, as is evident, for example, from the delay in the onset of surface precipitation (Figs. 5m and 6m).

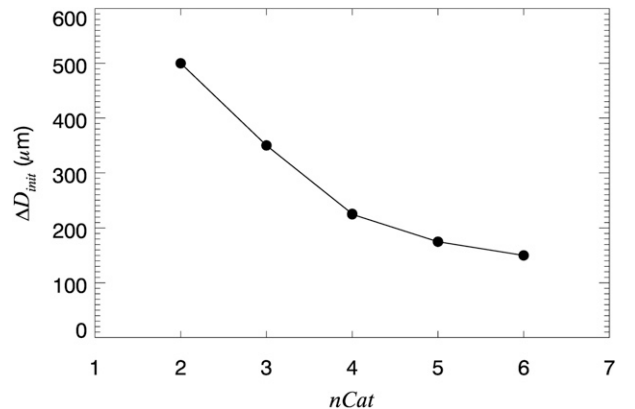


FIG. 7. Optimal values of  $\Delta D_{\text{init}}$  as function of  $n_{\text{Cat}}$ .

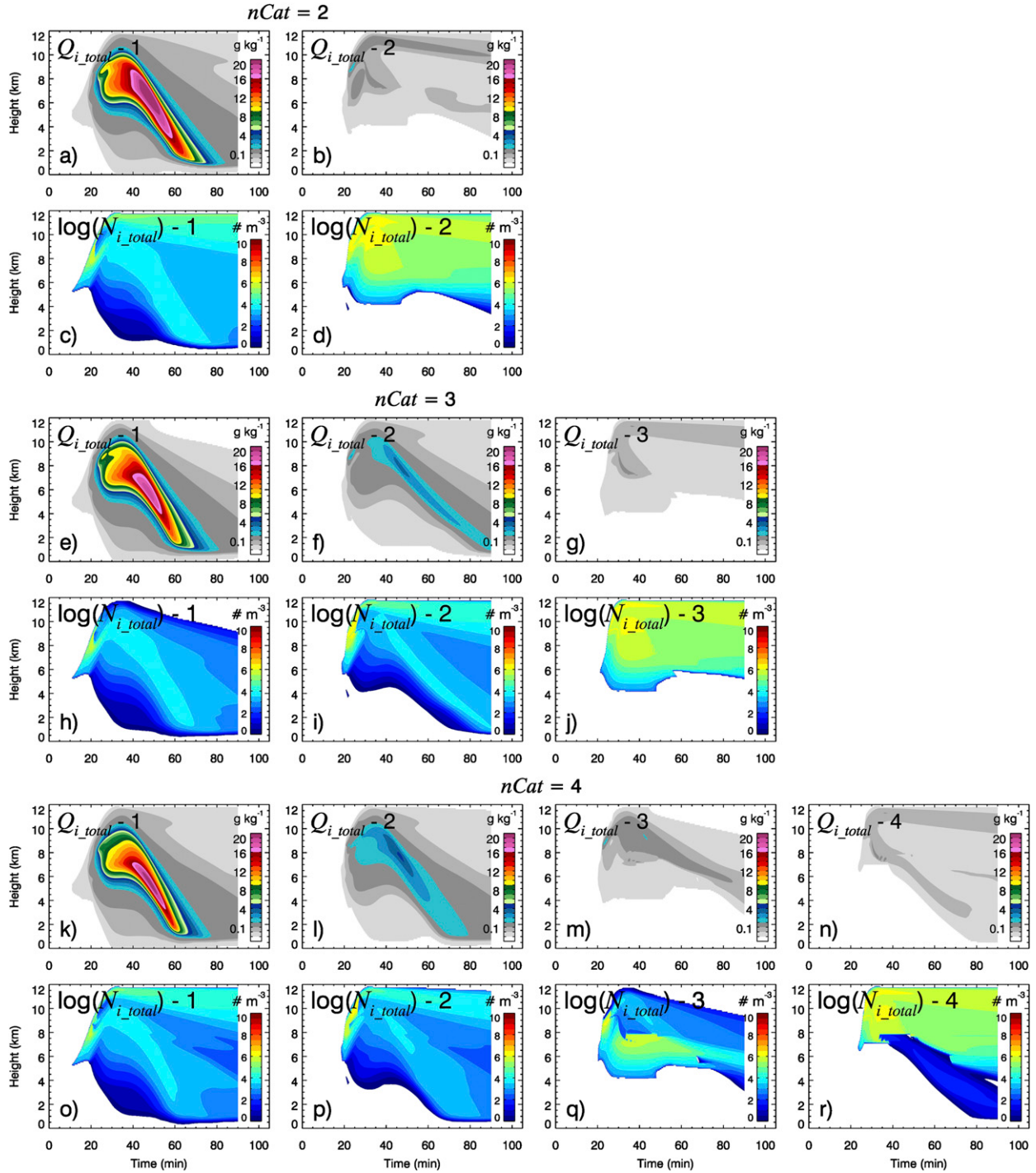


FIG. 8. (a),(b),(e)–(g),(k)–(n)  $Q_{i\_total}$  and (c),(d),(h)–(j),(o)–(r)  $N_{i\_total}$  for 1D kinematic model simulations with  $nCat = 2$ –4 using the modified  $\Delta D_{init} = f(nCat)$  and  $w_{max} = 10 \text{ m s}^{-1}$ .

The simulations were rerun for  $nCat = 1$  but now with rime splintering switched off. For  $nCat = 1$  (Fig. 12, column 1), the results are notably different compared to the control configuration with rime splintering on (Fig. 6, column 1). The local increase in  $N_{i\_total}$  at 4 km

(Fig. 6e) is gone with rime splintering off (Fig. 12e) and the result is a reduced dilution effect, evident from the ice mass sedimenting faster (Fig. 12a). The resulting precipitation rates (Fig. 12g), as well as the mass and reflectivity profiles, are in fact much closer to the  $nCat >$

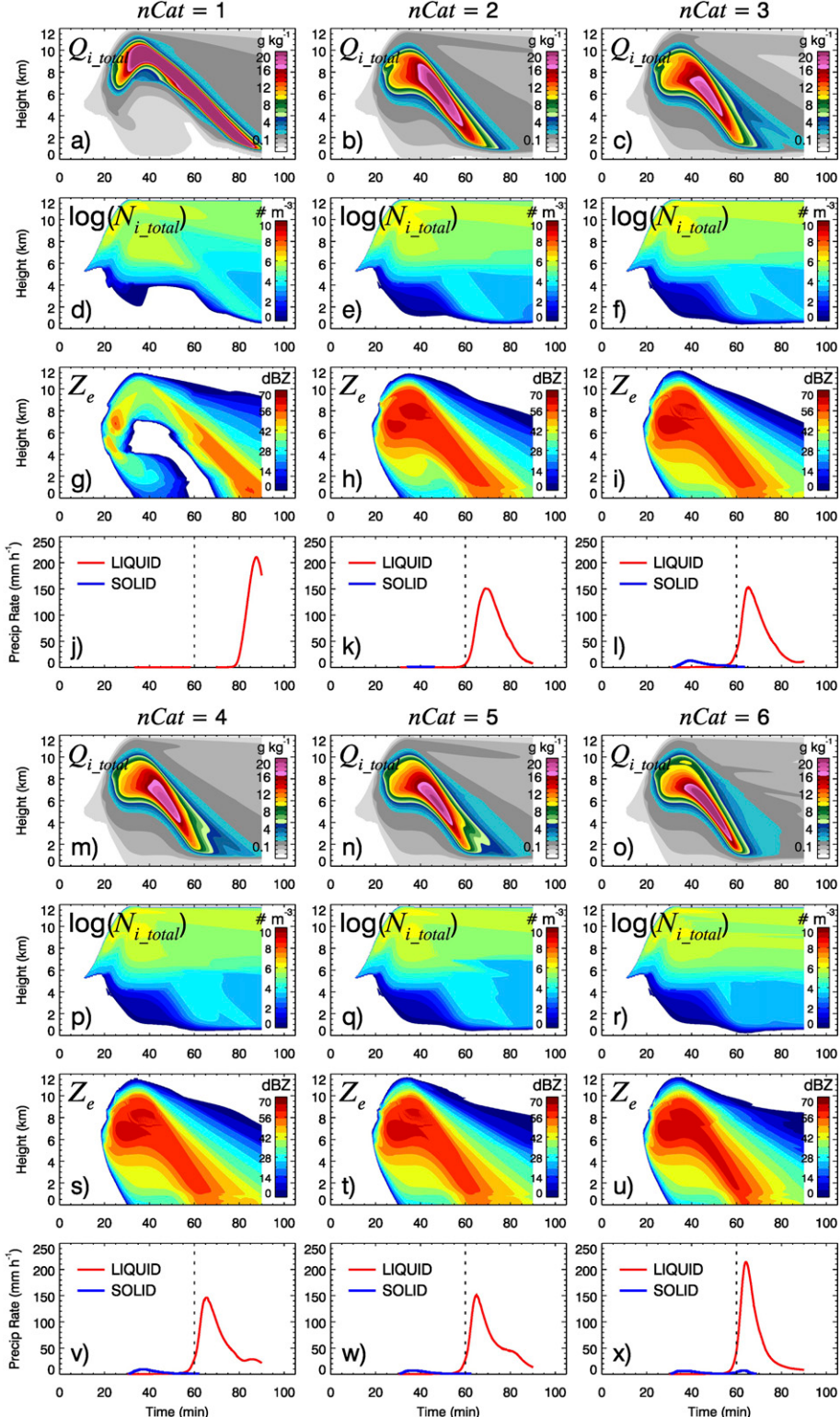
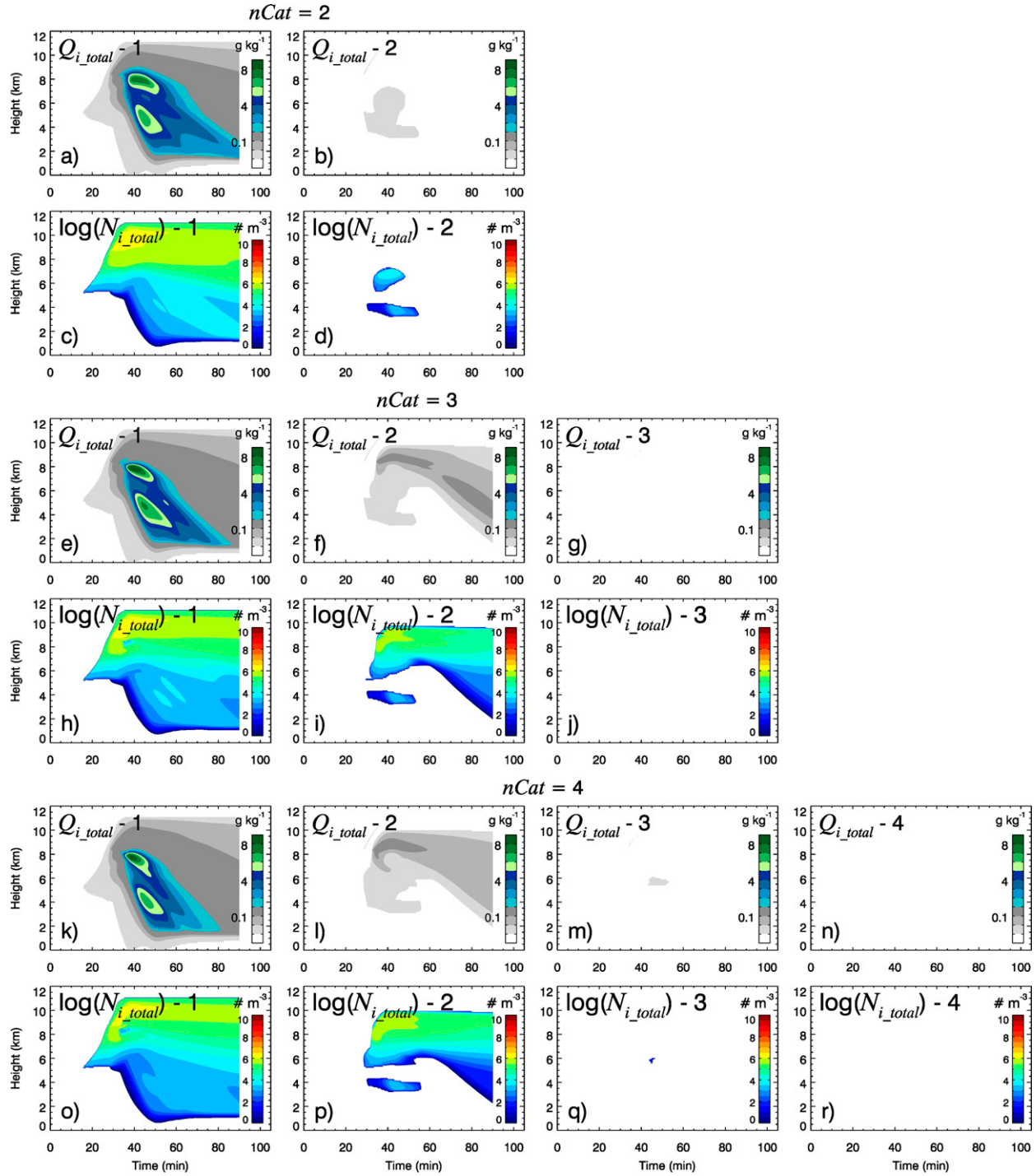


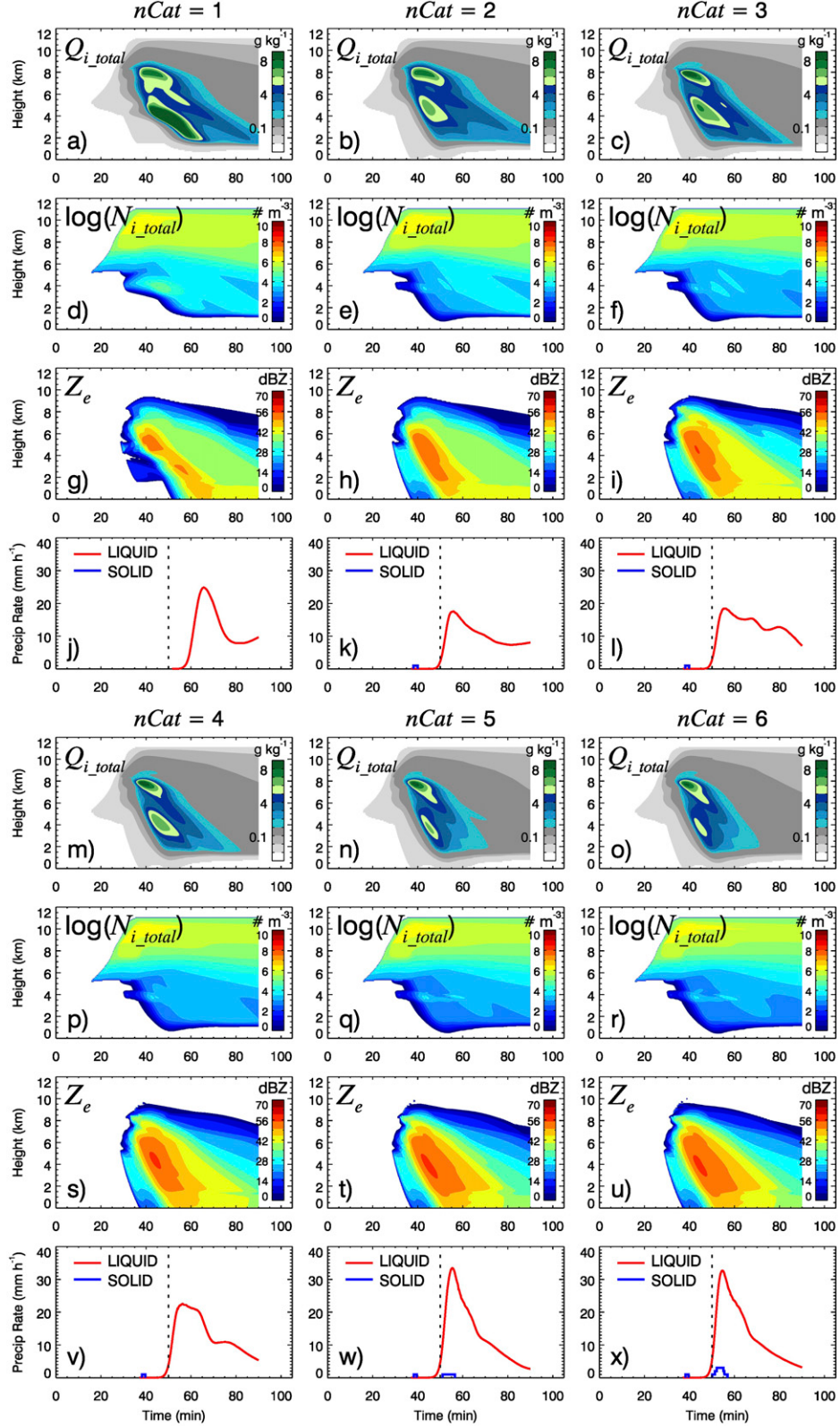
FIG. 9. Simulations using the modified  $\Delta D_{\text{init}} = f(n\text{Cat})$  and  $w_{\text{max}} = 10 \text{ m s}^{-1}$  for  $n\text{Cat} = 1\text{--}6$ . Panels indicate (a)–(c),(m)–(o)  $Q_{i\_total}$ , (d)–(f),(p)–(r)  $N_{i\_total}$ , (g)–(i),(s)–(u)  $Z_e$ , and (j)–(l),(v)–(x) surface precipitation rates.

FIG. 10. As in Fig. 8, but for  $w_{\max} = 3 \text{ m s}^{-1}$ .

3 simulations in Fig. 11. The results are similar for  $w_{\max} = 10 \text{ m s}^{-1}$  (not shown) but less pronounced.

This indicates, therefore, that for  $nCat = 1$  it is preferable overall to have rime splintering switched off, with the recognition that with a single ice-phase category (for any scheme) the dilution effect inherently limits the

complete and realistic simulation of all physical processes. However, it should also be recognized that the exclusion of rime splintering for  $nCat = 1$  ultimately does not really matter much to the overall simulation in term of the distribution of total ice mass, reflectivity, and surface precipitation. We remark that for the 3D

FIG. 11. As in Fig. 9, but for  $w_{\max} = 3 \text{ m s}^{-1}$ .

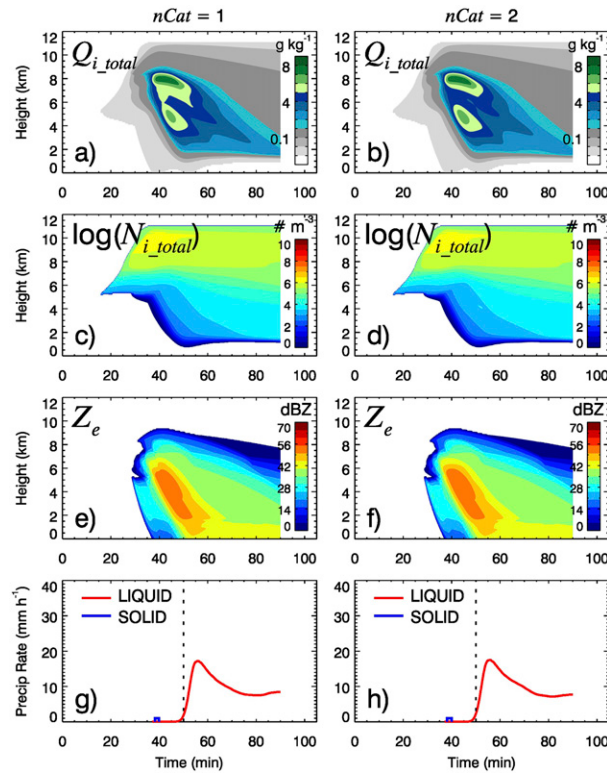


FIG. 12. Simulation with rime splintering off and  $w_{\max} = 3 \text{ m s}^{-1}$  for (a),(c),(e),(g) nCat = 1 and (b),(d),(f),(h) nCat = 2 of (top)–(bottom)  $Q_{i\_tot}$ ,  $N_{i\_tot}$ ,  $Z_e$ , and surface precipitation rates.

squall-line case presented in Part II and for an idealized 3D supercell simulation, inclusion of rime splintering using the one-category version of P3 was notably detrimental to the simulations, whereas switching off this process reduced the dilution problem in the updraft region and resulted in more realistic reflectivity structure of the convective cores. On the other hand, if inclusion of rime splintering is deemed important for a particular application, then nCat = 2 or higher is necessary. In short, using nCat  $\gg 1$  and including all parameterized processes is desirable since, in principle, it allows for a more realistic representation of ice-phase microphysics, but for some applications this added realism may be little more than aesthetic and the use of nCat = 2, or nCat = 1 with ice multiplication off, may be sufficient.

#### d. Effects of collection among ice categories

While we did not change any formulations for the microphysical processes when generalizing P3 to include multiple ice-phase categories, the process of ice “self-collection” was expanded to include collection among the various categories, as described in section 2b(2). This is a generalization of a preexisting parameterized process, but it does introduce a new

element of potential sensitivity in the multicategory scheme, specifically to the assumed collection efficiencies among particles with different categories ( $E_{i,k}$ ). Although all parametric equations representing microphysical processes include parameters or constants on which the growth/decay rates depend, the appropriate values of  $E_{i,k}$  are less understood (for all microphysics schemes) than other parameters. Sensitivity tests with the 1D model as well as 3D model simulations (not shown) indicate that the values of  $E_{i,k}$  can, in some situations, have a slight effect on the degree of dilution that occurs and on the sedimentation of mass in the higher ice categories (i.e.,  $n\text{Cat} \geq 2$ ), altering the distribution of mass in the different categories and the resulting surface precipitation. While the appropriate values of  $E_{i,k}$  may not be well understood, there is some observational evidence that there should be some temperature dependence on  $E_{i,k}$ , where the values are highest at temperatures near the triple point but become very low at temperatures below  $-20^\circ\text{C}$  (Pruppacher and Klett 1997).

Since the correct values of  $E_{i,k}$  are uncertain, the “merging” of categories due to collection in P3 may be underestimated or overestimated. However, poorly specified  $E_{i,k}$  with regards to collection among categories in P3 simply reduces the effectiveness of the categories for reducing dilution. At the extremes (zero collection among different categories or high collection efficiencies leading to excessive merging) result in, at the absolute worst, P3 reverting to its single-free-category configuration. Improvements to the specification of  $E_{i,k}$ , as well as other details of the various parameterized processes, will be the subject of ongoing development of the P3 scheme.

#### 4. Mesoscale model (3D) simulations

While the 1D kinematic model is useful for testing and to illustrate the behavior of the generalized scheme, the effects of multiple ice categories must ultimately be shown in a full 3D dynamical model. The multicategory version of P3 has been interfaced and tested in Environment Canada’s Global Environmental Multiscale (GEM; Côté et al. 1998) model and WRF (Skamarock and Klemp 2008). For consistency with Part II and to facilitate comparison to observations and other microphysics schemes reported therein, the quasi-idealized 3D squall-line case using WRF presented in that article was run with the multicategory P3. Three simulations were run using WRF v3.5.1 with a 1-km horizontal grid spacing and using the proposed P3 configuration described in the previous section, with nCat values of 1, 2, and 3, and ice multiplication off for nCat = 1 and on for all nCat  $> 1$ . Details of the case and of the model initial and boundary conditions are given in Part II.

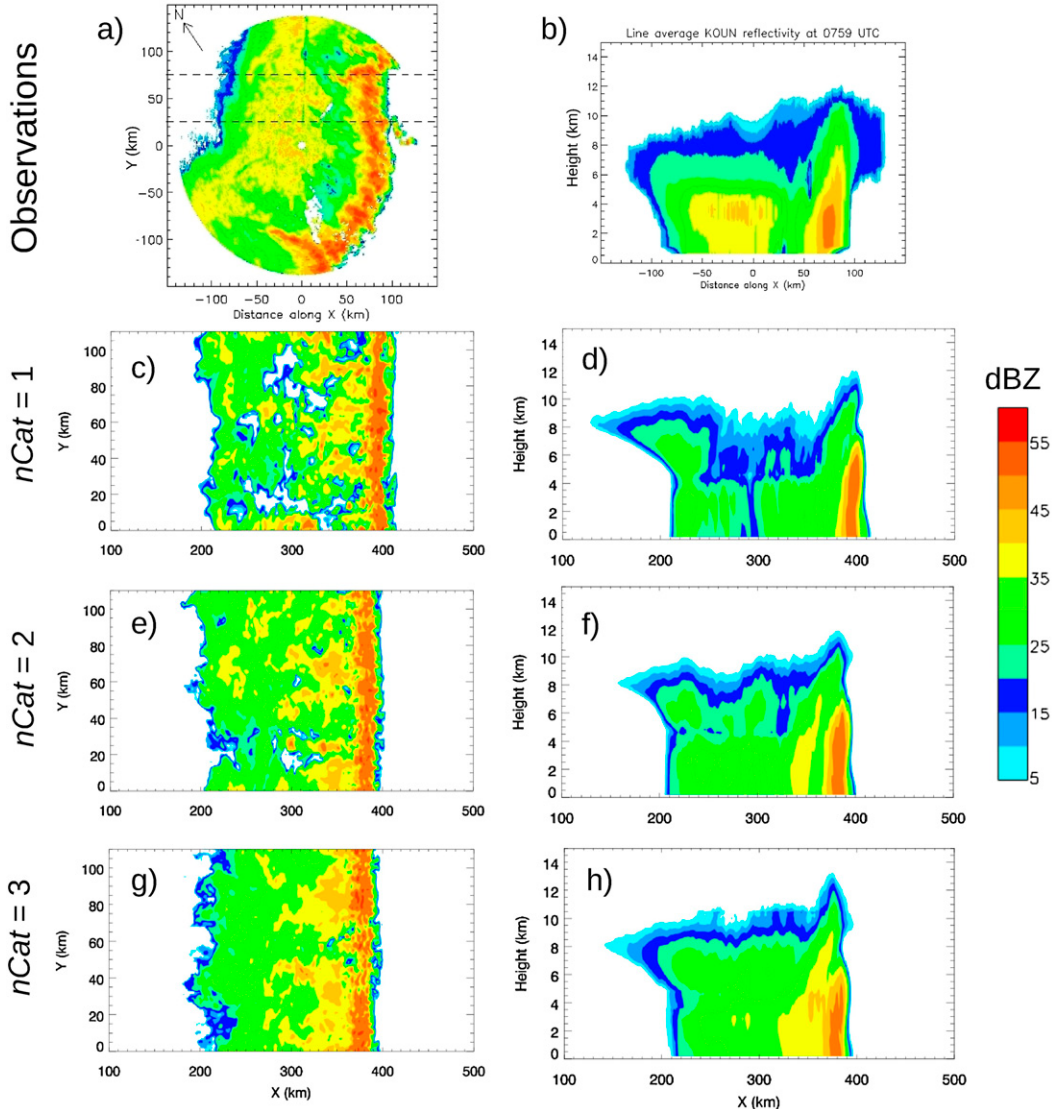


FIG. 13. (a),(b) Observed and (c)–(h) modeled radar reflectivity ( $Z_e$ ) from WRF simulations with  $nCat =$  (c),(d) 1; (e),(f) 2; and (g),(h) 3: (left) 1.1-km CAPPIs and (right) line-averaged vertical cross sections.

Following the model-observation comparison in Part II, Fig. 13 shows horizontal and vertical cross sections of the observed radar reflectivity and the equivalent model reflectivity ( $Z_e$ ) from each of the three simulations. Note that the results from the  $nCat = 1$  simulation (Figs. 13c and 13d) are somewhat different than the original single-category P3 results from Part II since several other minor modifications to the scheme have been made, in addition to the generalization to multicategory; however, this does not affect the interpretation of the effects of multiple ice categories. Each of the simulations capture the squall-line structure to a reasonable degree, though they differ somewhat. As  $nCat$  increases there is a “filling in” of some of the gaps in reflectivity in the

stratiform region that are present in the  $nCat = 1$  simulation near the surface. All of the runs have too-low reflectivity values in the stratiform region. This was the case for all the other microphysics schemes tested in Part II and is likely more related to the specific WRF configuration or initial conditions than the particular BMS. Overall, increasing  $nCat$  appears to result in a broadening of the high-reflectivity region immediately behind the convective core and an improvement to the overall structure of the stratiform region. Also, there appears to be a small dynamical effect of the number of ice categories as suggested by the slightly reduced propagation speed of the model storm with increased values of  $nCat$ , indicated by the location of the leading edge of convection.

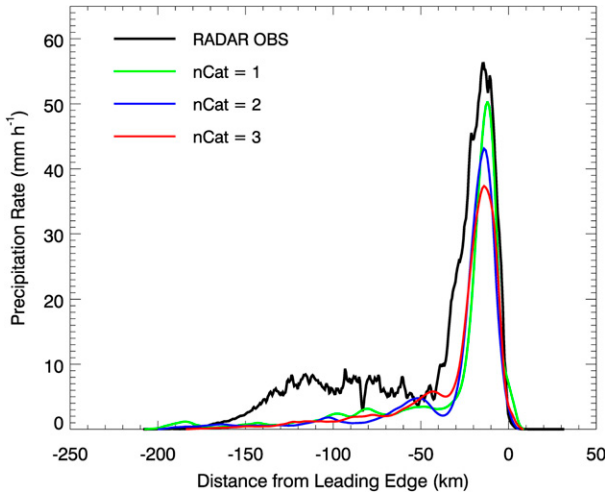


FIG. 14. Line-averaged cross sections of precipitation rate at  $\sim 1.1$  km AGL from WRF simulations with  $n\text{Cat} = 1$  (green), 2 (blue), and = 3 (red), and from radar retrieval (black).

The reflectivity patterns between the  $n\text{Cat} = 2$  and  $n\text{Cat} = 3$  simulations are different, however the differences are smaller than the differences between the  $n\text{Cat} = 1$  and  $n\text{Cat} = 2$  runs. Thus, although the model solution has not converged with  $n\text{Cat} = 3$ , it is reasonable to infer from Fig. 13 that the solution with  $n\text{Cat} = 4$  (not tested) would likely be very similar, consistent with the general findings from the 1D simulations. Given that this squall-line case is very strongly forced (with  $5900 \text{ J kg}^{-1}$  of CAPE in the initial conditions), the use of three ice categories is probably sufficient to establish effective convergence of the overall solution for most kilometer-scale model simulations using the multicategory P3.

The line-averaged near-surface precipitation rates after 6 h, corresponding to Fig. 13, are shown in Fig. 14. All configurations produce reasonable results and are consistent with the simulated reflectivity, with a broadening of the convective region for higher values of  $n\text{Cat}$  and a general underprediction in the stratiform region. The peak precipitation rates in the convective region decrease systematically with increasing, with values approximately 89%, 80%, and 68% of the observed peak rate for  $n\text{Cat}$  of 1, 2, and 3, respectively. All runs have precipitation rates of approximately one-third of the observed rates in the stratiform region (as did other schemes tested for this case; see Part II for details). Note that the radar-derived precipitation rates were well calibrated against rain gauges [see Morrison et al. (2012)].

Figure 15 shows vertical cross sections of some important bulk properties of the ice in each category for the  $n\text{Cat} = 3$  simulation. As with the 1D runs, the majority of the ice mass resides in category 1 (Fig. 15a) with

the least amount of mass in category 3 (Fig. 15c). Since this case is very strongly forced, with large quantities of liquid water available for riming in the convective region, consequently the properties of the various ice categories are similar at many locations. For example, at midlevels in the convective core (at 4–6 km,  $x \sim 380$  km) the values of  $F_{\text{rim}}$ ,  $D_i$ ,  $\rho_i$ , and  $V_i$  are similar indicating that each category is representing a similar type of dominant particle. The 1D tests suggest that a less strongly forced case would result in greater differences among the particle properties between categories. Even in this 3D case, however, there are some clear differences, illustrated in Table 3, which lists the property values of each category at three different locations in the storm, indicated by the symbols in Fig. 15d. The differences in property values indicate that in certain locations different types of particles are simulated by the different categories. In the anvil point, for example, ice in category 1 has  $F_{\text{rim}} \sim 0.2$ ,  $D_i \sim 67 \mu\text{m}$ ,  $\rho_i = 871 \text{ kg m}^{-3}$ , and  $V_i \sim 16 \text{ cm s}^{-1}$ , while the ice in category 2 is somewhat different, with  $F_{\text{rim}} \sim 0$ ,  $D_i \sim 167 \mu\text{m}$ ,  $\rho_i = 667 \text{ kg m}^{-3}$ , and  $V_i \sim 46 \text{ cm s}^{-1}$ . Although the ice in all categories can be described as being similar overall in the convective point, the bulk densities and fall speeds vary somewhat ( $483, 811, 667 \text{ kg m}^{-3}$  and  $6.12, 7.82$ , and  $7.05 \text{ m s}^{-1}$ , for categories, 1, 2, and 3, respectively). This spread in fall speed values contributes to the broadening of the reflectivity in the convective region and the overall filling in of gaps elsewhere.

These results do not indicate that running P3 with the highest number of ice categories will necessarily produce results closer to observations. In fact, the peak precipitation rates are too low for larger  $n\text{Cat}$ . The simulations illustrate simply that the generalized multicategory scheme appears to produce reasonable results in a realistic case using a 3D dynamical model, and that indeed it is now possible with P3 to simulate two or more distinctly different populations of ice particles at the same point in time and space. For the particular 3D case examined this did not have a large impact on the overall model solutions; however for other cases simulated using GEM (not shown) there were larger impacts including on the model dynamics. Future work will include closer examination of the effects and potential benefits of using multiple free ice categories for different types of real and idealized cases.

## 5. Discussion and conclusions

The P3 bulk microphysics scheme introduced in Part I has been generalized to allow for a user-specified number of free ice-phase categories. This modification removes the limitation in the original scheme described and tested

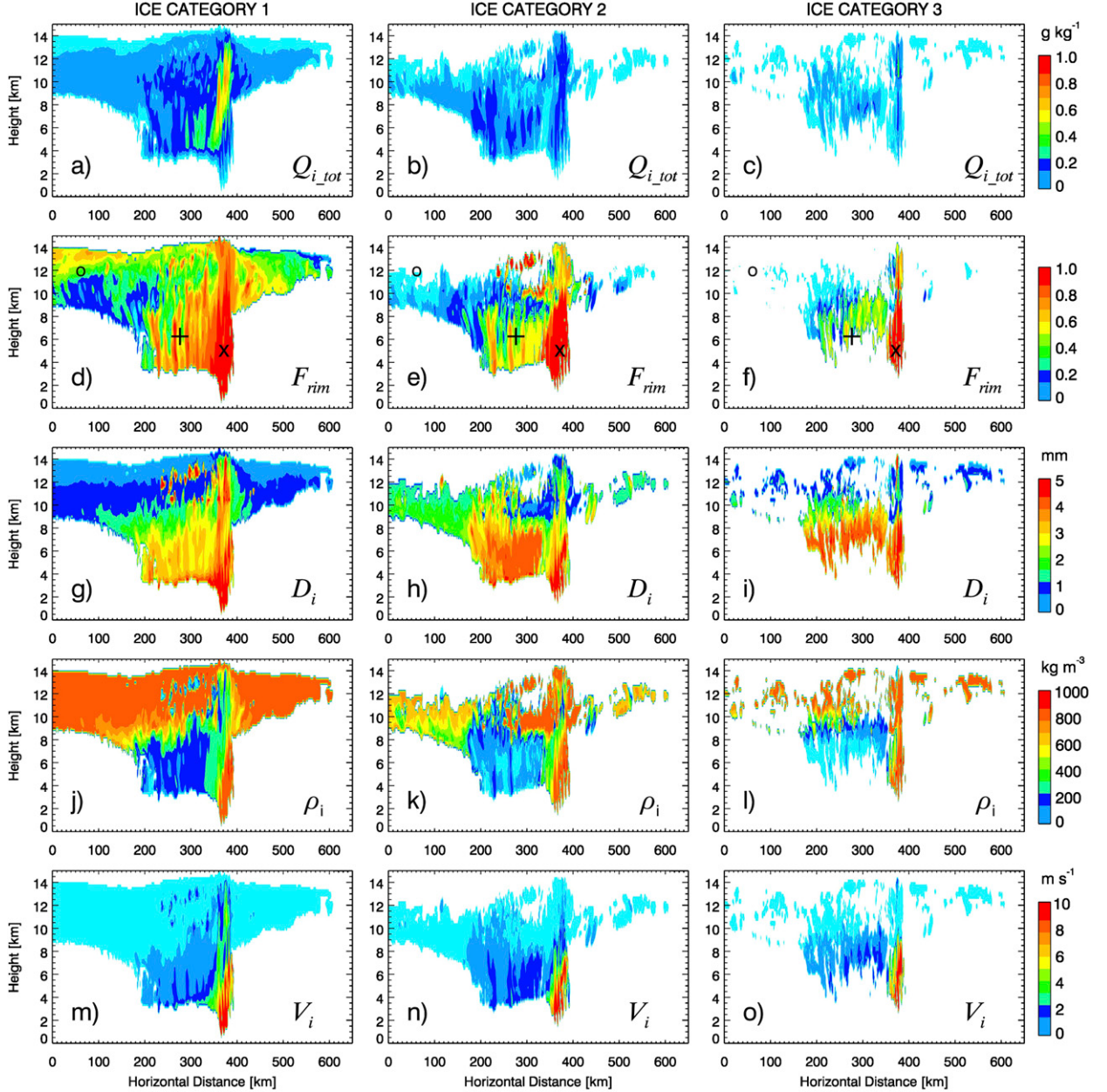


FIG. 15. Vertical cross sections (along  $y = 78$  km in Fig. 13g) from WRF simulation with  $n\text{Cat} = 3$  at integration time 6 h. Fields shown are (a)–(c)  $Q_{i\_tot}$ , (d)–(f)  $F_{rim}$ , (g)–(i)  $D_i$ , (j)–(l)  $\rho_i$ , and (m)–(o)  $V_i$  for ice categories (left) 1, (center) 2, and (right) 3.

in Part I and Part II that only allowed for populations of one type of ice particle to exist at a given point in time and space. Multiple ice populations can now be simulated and processes that promote this can now be included with minimal dilution of bulk physical properties. This scheme is the first to model ice-phase microphysics using multiple free categories. The generalization of the P3 scheme has been described and its behavior has been illustrated using an idealized 1D kinematic framework as well as with quasi-idealized 3D dynamical model simulations.

The 1D simulations illustrate that with an increased number of ice categories there is a reduction in the detrimental effects of bulk property dilution that occurs when few or one category is used. As more categories are added, the overall model solutions converge in terms of the overall simulated field values (i.e., total ice mass, number, reflectivity, surface precipitation rate), even though there may be differences in the way particle properties are distributed among the categories. When the forcing is stronger, there is an increased likelihood

TABLE 3. Particle properties for each ice category of the nCat = 3 simulation at the indicated locations corresponding to the points in Fig. 15.

	Ice category 1	Ice category 2	Ice category 3
Anvil (○)			
$q_{i,\text{tot}}$ ( $\text{g kg}^{-1}$ )	0.029	0.005	$4.0 \times 10^{-9}$
$F_{\text{rim}}$	0.195	0.042	0
$D_i$ (mm)	0.067	0.167	0.093
$\rho_i$ ( $\text{kg m}^{-3}$ )	871	667	801
$V_i$ ( $\text{m s}^{-1}$ )	0.16	0.46	0.28
Lower stratiform (+)			
$q_{i,\text{tot}}$ ( $\text{g kg}^{-1}$ )	0.038	0.064	$9.2 \times 10^{-5}$
$F_{\text{rim}}$	0.369	0.194	0
$D_i$ (mm)	1.84	4.50	3.93
$\rho_i$ ( $\text{kg m}^{-3}$ )	105	31.7	36.4
$V_i$ ( $\text{m s}^{-1}$ )	1.34	1.74	1.68
Convective core (×)			
$q_{i,\text{tot}}$ ( $\text{g kg}^{-1}$ )	1.282	0.080	0.002
$F_{\text{rim}}$	0.955	0.997	0.944
$D_i$ (mm)	4.64	4.19	4.54
$\rho_i$ ( $\text{kg m}^{-3}$ )	483	812	667
$V_i$ ( $\text{m s}^{-1}$ )	6.12	7.82	7.05

of a wider range of particle types and thus a greater number of categories is required to reach convergence. The 3D squall-line simulations exhibit the expected effects from the addition of ice categories, consistent with the results from the 1D model. These results illustrate the ability of P3 to simulate realistically not only a wide range of particle types in different parts of a convective system (as shown in Part I and Part II), but now also different types of particles at the same point in time and space. On the other hand, it is also evident that for the 3D squall line the nCat = 1 simulation (with rime splintering off) produced similar results to the multicategory runs.

One implication of the convergence behavior for practical applications is that for simulations of weather systems with strong environmental forcing, one would expect an increased ability to simulate the full range of microphysical processes by using a greater number of ice categories, whereas more weakly forced cases require fewer. Alternatively, if one wishes to simulate a weaker case with greater attention to ice particle details, more categories could be used but with a decreased  $\Delta D_{\text{init}}$  and more restrictive conditions for category merging such that all of the available ice categories are used, thereby minimizing the effects of dilution. If the degree of forcing is not known a priori, as is generally the case for NWP, then it would be recommended to use the maximum number of categories possible, dictated by available computational resources, with the initiation and the merging conditions calibrated such that all categories become populated for the more strongly forced cases.

Future work will include improving and testing alternative methods for determining the destination category of newly initiated ice and the merging of categories deemed to be sufficiently similar.

With the generalized P3 scheme now being capable of using any number of ice categories, it may be tempting to interpret this representation of the ice hydrometeors as converging toward a bin-resolving microphysics scheme for very large values of nCat. However, regardless of the value of nCat, P3 is still by definition a bulk scheme since each category, regardless of the number, represents a complete size distribution using a relatively small number of prognostic variables. With a further extension of the scheme to be triple moment, whereby the spectral dispersion of each category would thus be predicted and could be quite narrow, it could be argued that P3 would begin to resemble a Lagrangian particle model (e.g., Söhl and Kärcher 2010).

As was shown in Part II, the one-category P3 scheme is competitive with existing state-of-the-art BMSs not only in terms of simulation quality compared to observations but also computational cost. This is due partly to the extensive use of lookup tables with precomputed solutions to the process rate equations in the scheme itself but also because of the limited number of prognostic variables that are advected by the driving model. In the multicategory version, the number of prognostic variables is now increased by four for each additional ice-phase category, thus adding to the cost of advection. We remark in passing that the original motivation of the P3 approach was not focused on optimization; the intent was to provide a scientifically better approach to represent ice-phase microphysics in bulk schemes over the traditional approach of using predefined categories. Nevertheless, Morrison et al. (2015, manuscript submitted to *Mon. Wea. Rev.*) show that for each multi-variable hydrometeor category, it is only necessary to advect a lead variable (e.g., the mass mixing ratio) while the advective tendencies of the secondary variables (e.g., the number mixing ratio, etc.) can be computed by a linear scaling of the advective fluxes of the lead variable. This reduces the total computational cost of advection considerably. For P3, the potential impact in terms of computational savings is considerable given the relatively high ratio of secondary-to-lead advected variables for each ice-phase category [since it is only necessary to compute the regular advection of  $Q_{i,\text{tot}}(n)$ , while  $Q_{i,\text{rim}}(n)$ ,  $N_{i,\text{tot}}(n)$ , and  $B_{i,\text{rim}}(n)$  are secondary tracers].

Given the success of P3 so far in terms of overall simulation quality, the performance of the scheme in a kilometer-scale NWP context is ready to be tested. During the 2015 NOAA/HWT spring experiment, P3 was run with the one- and two-category configurations.

Tests have also been conducted in the context of Environment Canada's 2.5-km deterministic forecast system. In a future article, the results of these sets of tests and an evaluation of the performance of P3 in an operational NWP context will be presented.

**Acknowledgments.** We would like to acknowledge Sarah Tessendorf and Kyoko Ikeda for providing the observational datasets. We are grateful to Ted Mansell and two anonymous reviewers for their constructive comments. HM was partially supported by the U.S. DOE ASR DE-SC0008648, U.S. DOE ASR DE-SC0005336, subawarded through NASA NNX12AH90G, and the NSF Science and Technology Center for Multiscale Modeling of Atmospheric Processes (CMMAP), managed by Colorado State University under Cooperative Agreement ARM-0425247.

## REFERENCES

- Cheng, G., and M. English, 1983: A relationship between hailstone concentration and size. *J. Atmos. Sci.*, **40**, 204–213, doi:[10.1175/1520-0469\(1983\)040<204:ARBHCA>2.0.CO;2](https://doi.org/10.1175/1520-0469(1983)040<204:ARBHCA>2.0.CO;2).
- Côté, J., S. Gravel, A. Méthot, A. Patoine, M. Roch, and A. Staniforth, 1998: The operational CMC-MRB Global Environmental Multiscale (GEM) model. Part I: Design considerations and formulation. *Mon. Wea. Rev.*, **126**, 1373–1395, doi:[10.1175/1520-0493\(1998\)126<1373:TOCMGE>2.0.CO;2](https://doi.org/10.1175/1520-0493(1998)126<1373:TOCMGE>2.0.CO;2).
- Grabowski, W. W., and H. Morrison, 2008: Toward the mitigation of spurious cloud-edge supersaturation in cloud models. *Mon. Wea. Rev.*, **136**, 1224–1234, doi:[10.1175/2007MWR2283.1](https://doi.org/10.1175/2007MWR2283.1).
- Hallett, J., and S. C. Mossop, 1974: Production of secondary ice particles during the riming process. *Nature*, **249**, 26–28, doi:[10.1038/249026a0](https://doi.org/10.1038/249026a0).
- Harrington, J. Y., K. Sulia, and H. Morrison, 2013: A method for adaptive habit prediction in bulk microphysical models. Part I: Theoretical development. *J. Atmos. Sci.*, **70**, 349–364, doi:[10.1175/JAS-D-12-040.1](https://doi.org/10.1175/JAS-D-12-040.1).
- Hashino, T., and G. J. Tripoli, 2007: The Spectral Ice Habit Prediction System (SHIPS). Part I: Model description and simulation of the vapor deposition process. *J. Atmos. Sci.*, **64**, 2210–2237, doi:[10.1175/JAS3963.1](https://doi.org/10.1175/JAS3963.1).
- Li, J., and H. W. Barker, 2005: A radiation algorithm with correlated- $k$  distribution. Part I: Local thermal equilibrium. *J. Atmos. Sci.*, **62**, 286–309, doi:[10.1175/JAS-3396.1](https://doi.org/10.1175/JAS-3396.1).
- Lin, Y. L., R. Farley, and H. D. Orville, 1983: Bulk parameterization of the snow field in a cloud model. *J. Climate Appl. Meteor.*, **22**, 1065–1092, doi:[10.1175/1520-0450\(1983\)022<1065:BPOTSF>2.0.CO;2](https://doi.org/10.1175/1520-0450(1983)022<1065:BPOTSF>2.0.CO;2).
- Loftus, A. M., W. R. Cotton, and G. G. Carrio, 2014: A triple-moment hail bulk microphysics scheme. Part I: Description and initial evaluation. *Atmos. Res.*, **149**, 35–57, doi:[10.1016/j.atmosres.2014.05.013](https://doi.org/10.1016/j.atmosres.2014.05.013).
- Mansell, E. R., C. L. Ziegler, and E. C. Bruning, 2010: Simulated electrification of a small thunderstorm with two-moment bulk microphysics. *J. Atmos. Sci.*, **67**, 171–194, doi:[10.1175/2009JAS2965.1](https://doi.org/10.1175/2009JAS2965.1).
- Milbrandt, J. A., and M. K. Yau, 2005a: A multimoment bulk microphysics parameterization. Part I: Analysis of the role of the spectral shape parameter. *J. Atmos. Sci.*, **62**, 3051–3064, doi:[10.1175/JAS3534.1](https://doi.org/10.1175/JAS3534.1).
- , and —, 2005b: A multimoment bulk microphysics parameterization. Part II: A proposed three-moment closure and scheme description. *J. Atmos. Sci.*, **62**, 3065–3081, doi:[10.1175/JAS3535.1](https://doi.org/10.1175/JAS3535.1).
- , and H. Morrison, 2013: Prediction of graupel density in a bulk microphysics scheme. *J. Atmos. Sci.*, **70**, 410–429, doi:[10.1175/JAS-D-12-0204.1](https://doi.org/10.1175/JAS-D-12-0204.1).
- , J. Thériault, and R. Mo, 2014: Modeling the phase transition associated with melting snow in a 1D kinematic framework: Sensitivity to the microphysics. *Pure Appl. Geophys.*, **171**, 303–322, doi:[10.1007/s0024-012-0552-y](https://doi.org/10.1007/s0024-012-0552-y).
- Morrison, H., and J. A. Milbrandt, 2015: Parameterization of ice microphysics based on the prediction of bulk particle properties. Part I: Scheme description and idealized tests. *J. Atmos. Sci.*, **72**, 287–311, doi:[10.1175/JAS-D-14-0065.1](https://doi.org/10.1175/JAS-D-14-0065.1).
- , G. Thompson, and V. Tatarkii, 2009: Impact of cloud microphysics on the development of trailing stratiform precipitation in a simulated squall line: Comparison of one- and two-moment schemes. *Mon. Wea. Rev.*, **137**, 991–1007, doi:[10.1175/2008MWR2556.1](https://doi.org/10.1175/2008MWR2556.1).
- , S. Tessendorf, K. Ikeda, and G. Thompson, 2012: Sensitivity of a simulated midlatitude squall line to parameterization of raindrop breakup. *Mon. Wea. Rev.*, **140**, 2437–2460, doi:[10.1175/MWR-D-11-00283.1](https://doi.org/10.1175/MWR-D-11-00283.1).
- , J. A. Milbrandt, G. H. Bryan, K. Ikeda, S. A. Tessendorf, and G. Thompson, 2015: Parameterization of cloud microphysics based on the prediction of bulk ice particle properties. Part II: Case study comparisons with observations and other schemes. *J. Atmos. Sci.*, **72**, 312–339, doi:[10.1175/JAS-D-14-0066.1](https://doi.org/10.1175/JAS-D-14-0066.1).
- Pruppacher, H. R., and J. D. Klett, 1997: *Microphysics of Clouds and Precipitation*. 2nd ed. Kluwer Academic, 954 pp.
- Rutledge, S. A., and P. V. Hobbs, 1983: The mesoscale and microscale structure and organization of clouds and precipitation in midlatitude cyclones. VII: A model for the “seeder-feeder” process in warm-frontal rainbands. *J. Atmos. Sci.*, **40**, 1185–1206, doi:[10.1175/1520-0469\(1983\)040<1185:TMAMSA>2.0.CO;2](https://doi.org/10.1175/1520-0469(1983)040<1185:TMAMSA>2.0.CO;2).
- Seifert, A., and K. Beheng, 2006: A two-moment cloud microphysics parameterization for mixed-phase clouds. Part II: Maritime versus continental deep convective storms. *Meteor. Atmos. Phys.*, **92**, 67–88, doi:[10.1007/s00703-005-0113-3](https://doi.org/10.1007/s00703-005-0113-3).
- Skamarock, W. C., and J. B. Klemp, 2008: A time-split non-hydrostatic atmospheric model for research and forecasting applications. *J. Comput. Phys.*, **227**, 3465–3485, doi:[10.1016/j.jcp.2007.01.037](https://doi.org/10.1016/j.jcp.2007.01.037).
- Söhlch, I. K., and B. Kärcher, 2010: A large-eddy model for cirrus clouds with explicit aerosol and ice microphysics and Lagrangian ice particle tracking. *Quart. J. Roy. Meteor. Soc.*, **136**, 2074–2093, doi:[10.1002/qj.689](https://doi.org/10.1002/qj.689).
- Straka, J. M., and E. R. Mansell, 2005: A bulk microphysics parameterization with multiple ice precipitation categories. *J. Appl. Meteor.*, **44**, 445–466, doi:[10.1175/JAM2211.1](https://doi.org/10.1175/JAM2211.1).
- Thompson, G., P. R. Field, R. M. Rasmussen, and W. D. Hall, 2008: Explicit forecasts of winter precipitation using an improved bulk microphysics scheme. Part II: Implementation of a new snow parameterization. *Mon. Wea. Rev.*, **136**, 5095–5115, doi:[10.1175/2008MWR2387.1](https://doi.org/10.1175/2008MWR2387.1).
- Yuter, S. E., and R. A. Houze, 1995: Three-dimensional kinematic and microphysical evolution of Florida cumulonimbus. Part I: Spatial distribution of updrafts, downdrafts, and precipitation. *Mon. Wea. Rev.*, **123**, 1921–1940, doi:[10.1175/1520-0493\(1995\)123<1921:TDKAME>2.0.CO;2](https://doi.org/10.1175/1520-0493(1995)123<1921:TDKAME>2.0.CO;2).